

Ultrafast Electron Dynamics of Ultrathin Films of
Electrochemical Solvents Adsorbed on an Ag(111) Substrate

by

Matthew Lee Strader

B. A. (Wabash College) 2002

A dissertation submitted in partial satisfaction of the

requirements for the degree of

Doctor of Philosophy

in

Chemistry

in the

Graduate Division

of the

University of California, Berkeley

Committee in charge:

Professor Charles B. Harris, Chair

Professor Gabor A. Somorjai

Professor Roger W. Falcone

Spring 2008

The dissertation of Matthew Lee Strader is approved:

Chair	_____	Date	_____
	_____	Date	_____
	_____	Date	_____

University of California, Berkeley

Spring 2008

**Ultrafast Electron Dynamics of Ultrathin Films of
Electrochemical Solvents Adsorbed on an
Ag(111) Substrate**

Copyright © 2008

by

Matthew Lee Strader

Abstract

Ultrafast Electron Dynamics of Ultrathin Films of Electrochemical Solvents Adsorbed on an Ag(111) Substrate

by

Matthew Lee Strader
Doctor of Philosophy in Chemistry

University of California, Berkeley

Professor Charles B. Harris, Chair

Ultra-high vacuum (UHV) thin-film interfaces have been used to simulate the electrochemical double layer for decades. This formulation allows interfacial characterization methods to be employed that are incompatible with immersed electrode systems. Several UHV techniques can provide valuable energetic and structural information to complement immersed electrode results. UHV studies of electron population dynamics, energy relaxation, band structure and localization phenomena are commonplace for a large variety of metal-dielectric interfaces using two-photon photoemission (2PPE). 2PPE can access interfacial electronic states and track the dielectric response of adsorbed thin films.

Angle-resolved two-photon photoemission was used to study the energy relaxation, population decay and localization dynamics of image potential state (IPS) electrons in ultrathin films of dimethylsulfoxide (DMSO) on an Ag(111) substrate. Dynamic energy shifts of 50 ± 10 meV and 220 ± 10 meV were observed for $n=1$ IPS electrons at one monolayer and two monolayer coverages of DMSO, respectively. The difference in energy shifts is attributed to rotational hindrance of the molecular

dipole in the chemisorptive first monolayer. The finding confirms the proposed mechanism for the low differential capacitance of dimethylsulfoxide at noble metal interfaces in solution. A novel description of the IPS as a surface capacitance was formulated to facilitate comparisons with electrochemical systems. A direct observation has been made in vacuum to confirm a phenomenon postulated from bulk electrochemical measurements, and a connection between the fields of UHV and electrochemical surface science was reinforced.

Professor Charles B. Harris

Dissertation Committee Chair

To the mysteries of the universe
And to my wife,
Both of which make the daily grind
A little more interesting.

Contents

List of figures	v
List of tables	vii
1 Overview	1
2 Dynamic Interfacial Electronic Processes	2
2.1 Background	2
2.2 Ag(111) Band Structure and Interfacial States	2
2.2.1 Ag(111) Band Structure	2
2.2.2 Image Potential States	3
2.3 Angle-Resolved Two-Photon Photoemission	4
2.3.1 Pump-Probe Photoemission	4
2.3.2 Kinetic Energy Measurement using 2PPE	6
2.3.3 Static Workfunction Determination	6
2.3.4 Angle-Resolved Photoemission	7
2.4 Dynamic Interfacial Electronic Phenomena	9
2.4.1 Dynamic Population Relaxation	10
2.4.2 Dynamic Energy Relaxation	17
2.4.3 Dynamic Localization	21
2.5 Conclusion	24
3 Experimental Apparatus	25

3.1 Overview	25
3.2 Ultrathin Film Deposition	25
3.3 Mass Spectrometer	27
3.3.1 Default Specifications	27
3.3.2 Modifications for Thermal Desorption Spectroscopy	28
3.4 Substrate Temperature Control	34
3.5 Ultrafast Laser System	36
3.6 Systematic Error in 2PPE Dynamics: A Ghost Image	37
3.6.1 History of Symptoms	37
3.6.2 The Probe Pre-pulse and the Ghost Image	41
3.6.3 Pre-Pulse Detection and Elimination	44
3.6.4 Identification of Artifacts in Previously Collected Data	45
3.6.5 General Application to Data Collection Methodology	49
4 The Ultrafast Dynamics of Image Potential State Electrons at the Dimethylsulfoxide/Ag(111) Interface	51
4.1 Introduction	51
4.2 Experimental	53
4.3 Results	55
4.3.1 Coverage Identification	55
4.3.2 Monolayer Dynamics	59
4.3.3 Multilayer Dynamics	62
4.4 Discussion	67
4.4.1 Coverage Assignment: Comparisons to the Literature	67

4.4.2 Population Decay Times	68
4.4.3 Dynamic Energy Relaxation Mechanisms	69
4.4.4 The Image Potential State as a Capacitance	70
4.5 Advanced Fitting Procedures	79
4.5.1 Apparent Negative Effective Mass	79
4.5.2 Extraction of Delocalized State Dynamics	81
4.6 Conclusion	82
5 Implementation of Thermal Desorption Spectroscopy in the Current UHV Chamber	83
5.1 Thermal Desorption Spectroscopy	83
5.2 Component Synchronization for TPD Measurements	86
5.3 Theory of PID Temperature Control	87
5.3.1 Proportional Response	88
5.3.2 Integral Response	91
5.3.3. Derivative Response	93
5.4 Software Implementation of PID Temperature Control	96
5.4.1 Original Software Build	97
5.4.2 Current Software Build	98
5.5 Tuning the PID Controller to the Apparatus	101
5.6 Linear Temperature Ramping for TPD	102
5.7 Summary	103
References	104

List of Figures

2.1	Pulse sequences of 2PPE events	5
2.2	Angle-resolved detection of photoemission events	8
2.3	Intraband and interband relaxation mechanisms	12
2.4	IPS electron density above a thin film	14
2.5	Tunneling barrier to interfacial electron decay	16
2.6	Acceptance angle of apparatus in energy/momentum space	20
3.1	Modification to mass spectrometer for maximum penetration	29
3.2	Feulner cup	31
3.3	Interaction of Ag sample mount with the Feulner cup	32
3.4	Signaling of sample heating	35
3.5	Day-to-day variability of signal recurrence	38
3.6	Ghost dynamics on the clean Ag surface	40
3.7	Probe pulse profile in energy and time	42
3.8	Generation of dynamics from the pre-pulse	43
3.9	Prism compressor	46
3.10	Examples of ghost dynamics	48
4.1	Angle-resolved 2PPE dynamics of DMSO	54
4.2	2PPE dosing survey of DMSO	56
4.3	Dispersions of 1 ML of DMSO	58

4.4	Dynamic binding energy shift in 1 ML of DMSO	60
4.5	Population dynamics of 1 ML and 2 ML of DMSO	61
4.6	Dynamic binding energy shift of 1 ML and 2 ML of DMSO	63
4.7	Dispersions of 2 ML of DMSO	64
4.8	Capacitance model of the IPS	73
4.9	Electronic and molecular dielectric response	75
4.10	Long-time population decay of the 2 ML DMSO localized state	80
5.1	TPD spectrum of 2 – 3 ML of butanol	84
5.2	Numerical simulations of P controllers	90
5.3	Numerical simulations of PI controllers	92
5.4	Numerical simulations of PID controllers	95

List of Tables

4.1 Linear slopes of n=1 IPS energy relaxation for 1 ML of DMSO at various collection angles	62
4.2 Average of rise and decay times of n=1 IPS for 2 ML of DMSO	66
4.3 Electrochemical Model Predictions for 1 ML and 2 ML of DMSO	76

Acknowledgements

I would like to acknowledge all those who helped me through my time in graduate school. You know who you are, and I sincerely appreciate every instance of aid and friendship. “*What a long, strange trip it’s been.*” – The Grateful Dead

However, there are those that demand more specific acknowledgement. Therefore, this work was supported by the Director, Office of Science, Office of Basic Energy Sciences, Chemical Sciences Division of the U. S. Department of Energy, under Contract No. DE-AC02-05CH11231. The author acknowledges NSF support for specialized equipment used in the experiments herein.

Chapter 1: Overview

Ultrafast spectroscopy permits the study of a wide range of physical processes on the femtosecond to nanosecond timescale. Many electronic processes occur on this timescale and can be investigated with visible and ultraviolet radiation. Specifically, the phenomena of electron solvation, localization, interband relaxation and electronic cooling all occur at timescales which can be studied with ultrafast methods. These phenomena affect areas as diverse as the function of photovoltaic devices through the dynamics of charge injection to the rate of charge transfer reactions through solvation dynamics. Study of dynamic, ultrafast electronic phenomena on a fundamental level yields insight into a variety of physical questions.

The ultrahigh vacuum environment enables the study of ultrafast electron dynamics at the interface with angle-resolved, two-photon photoemission spectroscopy (2PPE). An assortment of interfaces can be produced by the deposition of an ultrathin film (< 10 monolayers) on a metal, single-crystal substrate. UHV thin-film interfaces have been used to simulate the electrochemical double layer for decades. This formulation allows interfacial characterization methods to be employed that are incompatible with immersed electrode systems. However, the investigation of thin films in UHV has not been conducted in the context of electrochemical relevance. Specifically, the ultrafast, interfacial dielectric response of common electrochemical solvents can be studied with angle-resolved 2PPE. The following work focuses on the use of UHV thin films as models for the electrochemical interface in solution.

Chapter 2: Dynamic Interfacial Electronic Processes

2.1 Background

Electronic phenomena occurring in homogeneous materials have been well-characterized in the literature. However, electronic processes occurring at interfaces between materials are still a subject of interest. The broad range of systems that depend on interfacial electronic processes include the disciplines of electrochemistry, photovoltaics and catalysis. Ultra-high vacuum (UHV) techniques have been demonstrated to be quite effective for the investigation and characterization of interfaces.¹ Two-photon photoemission (2PPE) is one such UHV technique employed to study interfacial electronic processes such as electron population dynamics, energy relaxation, band structure and localization phenomena.²⁻⁶ In 2PPE experiments, the interface to be studied is often formed by depositing ultrathin films, i.e. 1-10 monolayers (ML), of material on a crystalline substrate.

2.2 Ag(111) Band Structure and Interfacial States

2.2.1 Ag(111) Band Structure

In the current experiments, the substrate used is the [111] face of Ag single crystal. The substrate band structure and supported electronic states are relevant for

photoemission experiments and are discussed further. The Ag(111) crystal face has a workfunction of 4.56 eV.⁷ The bulk band structure projected onto the Ag(111) face results in a 4.15 eV band gap with the valence band edge located 0.30 eV below the Fermi energy at the $\bar{\Gamma}$ point.⁷⁻⁹ An initially occupied surface state is located 0.12 eV below the Fermi level.¹⁰ Additionally, a peak is observed from an *sp* band bulk transition and is here referred to as the Miller-McMahon-Chiang (MMC) state.^{11, 12}

2.2.2 Image Potential States

The initially unoccupied series of image potential states (IPS's) are also observed in 2PPE experiments from the Ag(111) surface. The hydrogenic progression of IPS's arises from the attractive, coulombic potential between an electron and the polarization it induces at a metal surface. The IPS binding energy is defined by Equation 2.1:

$$E_n = -\frac{.85\text{eV}}{(n+a)^2} + V_0 \quad (2.1)$$

where n represents the principle quantum number, V_0 represents the vacuum energy and a represents the quantum defect parameter.¹³ Experimentally, $n=1$ and $n=2$ image potential states have been observed at the Ag(111) interface with energies of 0.77 eV and 0.23 eV below the vacuum energy, respectively. The expectation values for $n=1$ and $n=2$ IPS electrons are 3 Å and 12 Å, respectively. Due to the proximity of IPS's to the surface, they serve as a useful probe of interfacial electronic properties and are the focus of the photoemission experiments reported in this work.

2.3 Angle-Resolved Two-photon Photoemission

2.3.1 Pump-Probe Photoemission

In the current 2PPE experiment, a sub-hundred femtosecond pulse and its second harmonic impinge upon a silver substrate with a controllable time delay of femtoseconds to picoseconds between pulses. Figure 2.1 illustrates the relevant energies and possible sequences of events in 2PPE. Initially, an electron is excited (pumped) from below the Fermi level of the metal substrate into an intermediate state by a photon from the first pulse. Subsequently, the electron is photoemitted (probed) by a photon from the second pulse, and the kinetic energy of the electron is recorded. A kinetic energy spectrum for a particular pump-probe delay can be formed from a histogram of $\sim 10^5$ photoemission events plotted by kinetic energy. Peaks in the spectrum correspond to initial, intermediate or final state resonances. The controllable time delay between pump and probe allows for the study of the intermediate state as a function of time.

By noting that the second harmonic (UV) pulse is constrained to an energy of twice the fundamental (vis), UV pumped/vis probed, vis pumped/UV probed, and virtual intermediate sequences can be identified by a slope of one, two or three in a plot of photoemitted electron kinetic energy with respect to fundamental pulse energy. The binding energy of an intermediate state can be calculated from the photoemitted

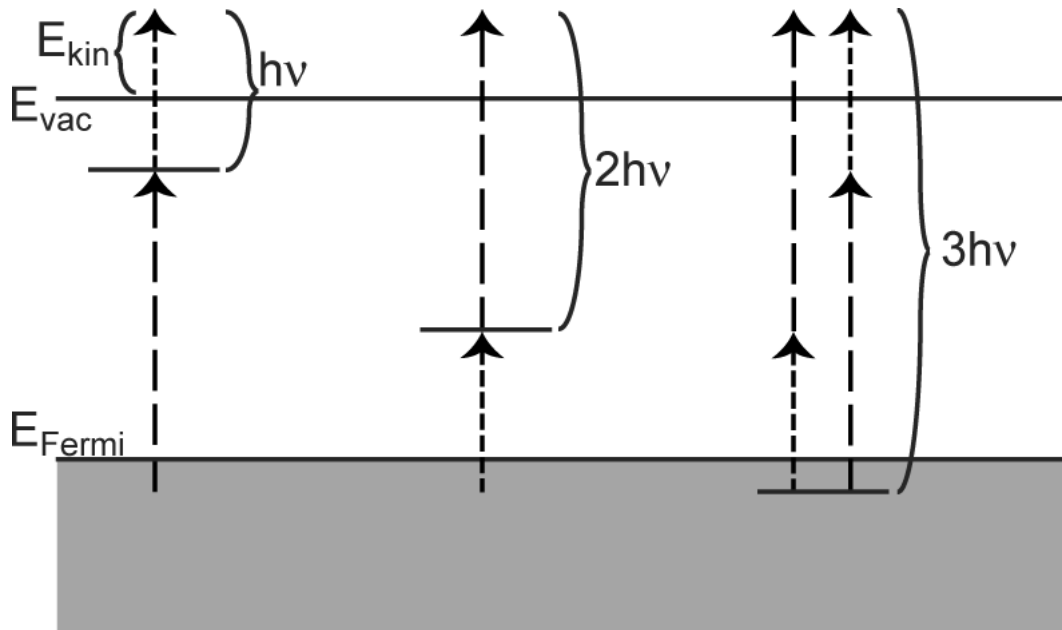


Figure 2.1: An energy diagram is presented depicting the various pulse sequences of 2PPE. A fundamental pulse wavelength of energy $h\nu$ or its second harmonic are shown exciting an electron from below the Fermi level (E_{Fermi}) to an unoccupied intermediate (left and middle) or virtual intermediate (right) electronic state. The probe pulse subsequently excites the electron from the intermediate state to an energy above the vacuum level (E_{vac}), which photoemits the electron with a kinetic energy of E_{kin} .

electron kinetic energy by subtracting the probe photon energy.

2.3.2 Kinetic Energy Measurement using 2PPE

The kinetic energy of photoemitted electrons is determined with a time-of-flight (TOF) analysis using microchannel plates (MCP's), described elsewhere.¹⁴ The energy resolution from TOF detection is ± 15 meV. Acquisition of kinetic energy spectra requires tunable UV/vis photon energies to 1) populate the desired intermediate states, 2) to avoid exceeding the workfunction, and 3) to ascertain the pulse sequence and, consequently, intermediate state binding energy as described above. The tunable range of visible and UV photon energies using the current experimental setup is 1.65 – 2.50 eV and 3.30 – 5.00 eV, respectively. However, the constraint of the UV photon energy to twice that of the visible becomes important in congested kinetic energy spectra of four or more features.¹⁵ A second, independently tunable light source would be of great use to resolve overlapping peaks, especially when the overlapped features are photoemitted with different pulse sequences.¹⁶

2.3.3 Static Workfunction Determination

A contact potential is formed from the workfunction mismatch between the Ag substrate and the MCP's.¹⁷ The resulting surface charge will create an electric field along the substrate to detector axis. The kinetic energy of photoemitted electrons traveling along this axis will be modified by the electric field. A potential bias is

applied to a wire mesh grid located directly in front of the MCP's. The bias corrects the workfunction mismatch and creates a field-free region for electron travel. However, growth of thin films on the substrate modifies the substrate workfunction, and the applied bias must be adjusted.

The correct, applied grid bias potential for a thin film coverage can be determined when multiple IPS's are present. The energy difference between image potential states and Equation 2.1 can be used to solve for a single quantum defect parameter a under the assumption that a varies insignificantly between image potential states.¹⁷ The vacuum energy can thus be obtained and the grid bias can be determined. The contact potential shift upon thin film adsorption corresponds directly to the workfunction shift as determined by the grid bias adjustment, from which a thin film workfunction can be determined.

2.3.4 Angle Resolved Photoemission

The electron momentum in the plane parallel to the substrate/vacuum interface ($\hbar k_{\parallel}$) is conserved upon photoemission.¹⁷ This parallel momentum contribution to the photoemitted electron determines the photoemission angle, as shown in Figure 2.2. When the angle of the detector with respect to the surface normal (θ) is known, the parallel momentum of the electron can be determined from the kinetic energy (E_{kin}). Equation 2.2 states the relationship:

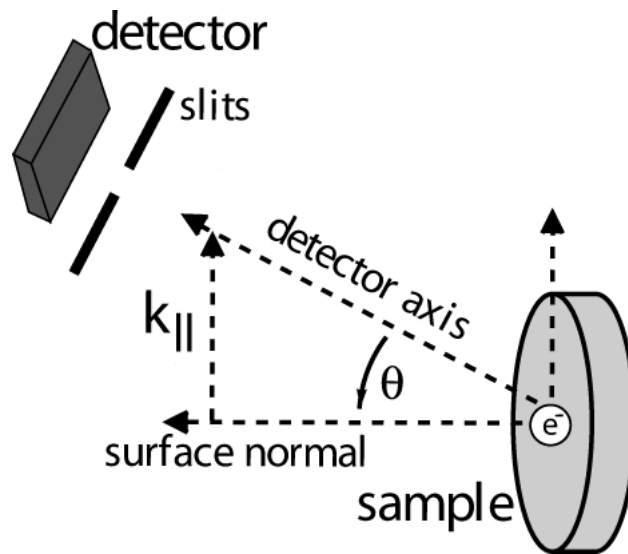


Figure 2.2: The path of a photoemitted electron is depicted with respect to the substrate-detector alignment. The parallel momentum contribution from $k_{||}$ to the photoemission angle θ is shown.

$$k_{\parallel} = \frac{\sqrt{2m_e E_{kin}}}{\eta} \sin \theta \quad (2.2)$$

where m_e is the mass of a free electron. The wavevector-dependent kinetic energy ($E_{kin}(\mathbf{k}_{\parallel})$) can be collected at a range of photoemission angles to construct a dispersion relation, expressed in Equation 2.3:

$$E_{kin}(k_{\parallel}) = E_{kin}(0) + \frac{\eta^2 k_{\parallel}^2}{2m^*} \quad (2.3)$$

where m^* represents the effective mass of the electron in the intermediate state. The electron in the intermediate state is coupled to the band structure at the interface, and its effective mass can differ from that of a free electron. Angle-resolved photoemission allows for determination of the band mass of initially occupied and unoccupied interfacial electronic states.

Interfacial electrons have been observed to strongly localize in energetically corrugated environments.^{4, 18, 19} An electron in a localized state does not move significantly in the plane parallel to the surface,²⁰ and it is consequently nondispersive. The description of these electrons as plane waves with a unique \mathbf{k}_{\parallel} is no longer accurate. The wavefunction of a spatially localized electron can be better represented as a sum of plane waves as in Equation 2.4:

$$\psi_{loc} = \sum_{k_{\parallel}} c_{k_{\parallel}} \psi_{k_{\parallel}} \quad (2.4)$$

where the coefficients c satisfy the normalization condition of Equation 2.5:

$$1 = \sum_{k_{\parallel}} c_{k_{\parallel}}^2 \quad (2.5)$$

While the photoemission angle does not accurately reflect the momentum of the state, the distribution of the coefficients does describe the distribution of the localized state in \mathbf{k} -space. The \mathbf{k} -space width is related to the wavefunction size distribution in coordinate space, and a rough estimate of its size can be made by assuming a Gaussian wavefunction shape. It can be shown that the Gaussian full width at half maximum (FWHM) in coordinate and momentum space are related by a Fourier transform given by Equation 2.6.²⁰

$$\Delta x_{FWHM} = \frac{4 \ln 2}{\Delta k_{FWHM}} \quad (2.6)$$

2.4 Dynamic Interfacial Electronic Phenomena

Pump-probe techniques are commonly utilized to study dynamic processes. The dependence of observables on the pump-probe delay interval leads to insight concerning the mechanistic details of physical processes. In the case of 2PPE measurements, a number of observables can be studied as a function of time. Dynamic changes in the population, energy and dispersion of a pumped, intermediate state elucidate the decay, solvation and localization mechanisms of interfacial electrons.

Temporal measurements are limited by two considerations. The first consideration results from the translation stage used to delay the visible pulse with respect to the UV. The stage uses 1 μm step sizes, resulting in minimum pump-probe delay increment of 6.7 fs. The range of motion of the translation stage is 25 cm and

consequently 1.7 ns, which has never presented a problem. The second consideration is the temporal width of the excitation pulses. The visible pulse autocorrelates to a full width at half maximum (FWHM) of 60 – 100 fs, and the UV/vis cross-correlation is between 100 -150 fs. The width of these pulses contributes a temporal uncertainty of at least ± 20 fs to all time-dependent measurements.

2.4.1 Dynamic Population Relaxation

The absolute intensity of a feature in a kinetic energy spectrum depends on many factors: intensity, focus, spatial overlap and temporal compression of pump and probe beams, surface and adsorbed layer cleanliness, and the non-unity probability of photoemitted-electron detection by the MCP/electronics assembly. A number of these quantities change from experiment to experiment and can be difficult to thoroughly characterize, and the absolute intensity is consequently of little quantitative value. However, within a single experiment the experimental apparatus is quite stable, and the relative intensity of spectral features collected during an experiment reflects the relative population of various states. Analysis of population dynamics yields a great deal of information about population relaxation mechanisms.

Interband transitions

Populations of electronic states can relax through varied intraband and interband relaxation mechanisms, shown in Figure 2.3. The dominant, long-time population relaxation mechanism of IPS electrons is that of tunneling into the Ag substrate. The other interband transition of interest in this work is that of dynamic

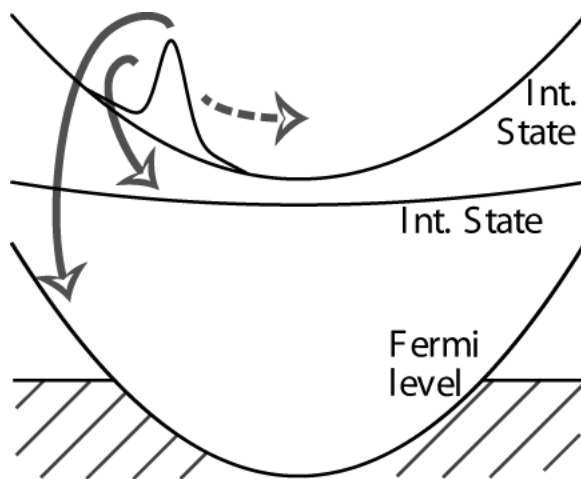


Figure 2.3: Intraband (dotted) and interband (solid) decay mechanisms of an excited state electron wavefunction (Gaussian wavepacket). Unprobed electrons will eventually relax to states below the Fermi level.

localization (Section 2.4.3). The relaxation rate of the transition to the substrate is affected by a number of factors: the average distance of the IPS electron from the surface,²¹ the energy overlap of the IPS electronic state with the substrate band structure²² and the wavefunction overlap of the IPS electron with the final state.²³

The effect of the distance of an IPS electron from the surface can be described in the theoretical framework of the classical round trip time.²¹ Here, the electron is described as oscillating between the classical turning point and the metal surface, from which it is reflected. The period of the oscillation is energy-dependent. Calculation of round trip times for the quantized IPS energies yields round trip times proportional to n^3 . To restate, the lifetime of IPS's depends on the distance of the states from the surface. Such a dependence is found in the IPS's of the Ag(111) surface with $n \geq 2$.²²

The distance dependence of IPS lifetimes aids in the characterization of ultrathin films deposited on the substrate. Materials with negative electron affinities will push the IPS wavefunction towards the vacuum interface. Thicker coverages of material will push the expectation value further from the surface, as illustrated in Figure 2.4. Lifetime effects have been used to assist coverage assignment in a number of studies. Furthermore, a lifetime strongly dependent on film thickness is an indication that the electron resides primarily on the adsorbate/vacuum edge of the film and not in the adsorbed layer.^{13, 24, 25}

Population relaxation can also be affected by the substrate band structure. The Ag(111) $n = 1$ IPS lifetime ($\tau = 40$ fs) deviates from the n^3 dependence of higher quantum number IPS's and is longer than the $n = 2$ IPS lifetime ($\tau = 25$ fs).²² This

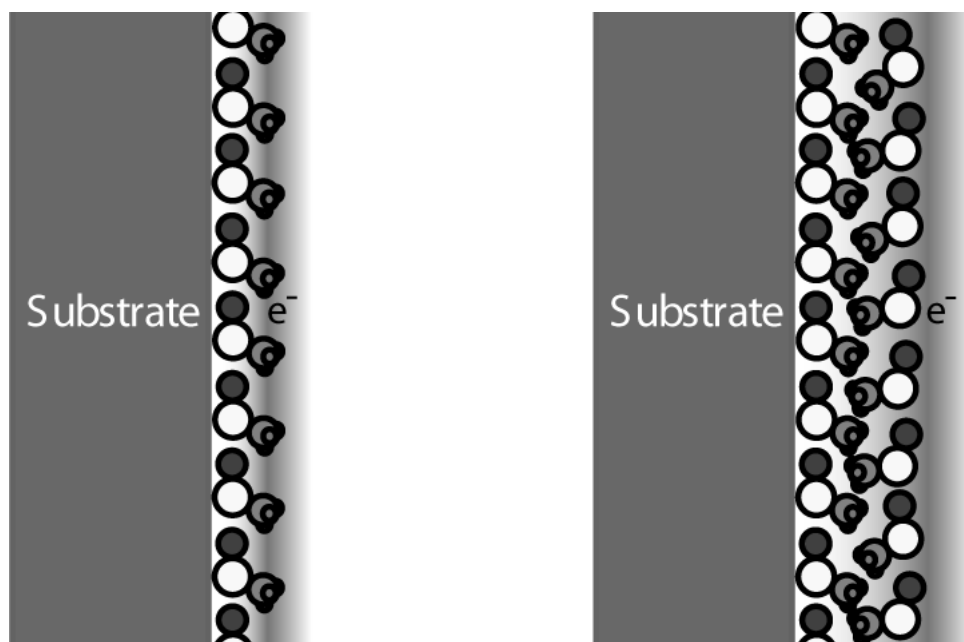


Figure 2.4: The effect of adsorbed ultrathin films of different thicknesses on the electron probability density. The film depicted is dimethylsulfoxide. An electron delocalized in the plane parallel to the metal is represented by the shaded area. Note: Information on the structure of multilayer DMSO films is not reported in the literature. Consequently, the illustration of DMSO molecules exposed to the vacuum interface in the right panel is not meant to imply a true interfacial structure.

anomaly illustrates the effect that the energy overlap of the IPS with the substrate band structure has on state lifetimes. Image potential states with $n \geq 2$ are resonant with the Ag(111) conduction band while the $n = 1$ IPS resides in the band gap. The lifetime of $n = 1$ IPS electrons are lengthened with respect to higher quantum number IPS's by the lack of resonance with substrate electronic states, and the energetic position of a state with respect to the substrate band structure must be considered when analyzing population lifetimes.

Population relaxation studies have also identified *dynamic* mechanisms which further lengthen intermediate state lifetimes. Electrons can interact with adsorbed thin films to reduce the energy of the system (Section 2.4.2). The interaction is thought to create a perturbation in the Coulomb potential, which forms a tunneling barrier and decouples the electron wavefunction from the substrate.²³ A schematic representation of this effect is given in Figure 2.5. An inhomogeneous distribution of conduction band electrons in thin films of ice deposited on Cu(111) and Ru(001) have shown this effect. The peak inhomogeneity arises from a distribution of trap sites which stabilize the electrons to various degrees (Section 2.4.3). A dynamic shift in peak energy can be attributed to differing decay rates between elements in the inhomogeneous distribution. Stronger trapping (i.e. larger energy relaxation) causes deeper well formation and stronger decoupling of electron wavefunctions from the substrate. A model calculation using a rectangular barrier of variable thickness has been used to describe this effect in ice thin films.²³

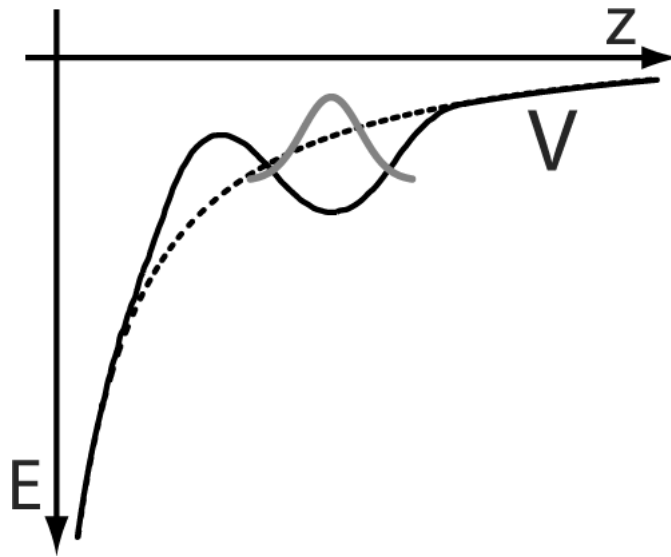


Figure 2.5: The unperturbed Coulomb potential (dotted) and the Coulomb potential perturbed by thin film reorganization (black) are plotted as a function of distance from the surface. The perturbation creates a barrier between the electron wavefunction (grey) and the surface at $z = 0$, through which the electron must tunnel to decay to the substrate.

Intraband Transitions

On timescales shorter than the decay of electrons to the substrate, intraband transitions can be observed. Both intraband and interband relaxation are illustrated in Figure 2.3. Intraband relaxation can be understood as electronic cooling.²⁵ Excitation to an intermediate state by a femtosecond laser pulse produces an initially hot electronic distribution, which is cooled by scattering events on the timescale of hundreds of femtoseconds to the temperature of the substrate. The population dynamics display parallel momentum-dependent rise and decay times as a direct result of cooling. The population at high parallel momenta decays rapidly as the hot distribution cools. In contrast, the population at low parallel momenta initially rises as population is transferred from higher momentum states. Whenever population decay to the substrate occurs on a comparable or longer timescale than electronic cooling,²⁵ the effects on population dynamics are observed. However, quantitative characterization of cooling timescales has proved intractable when multiple interband relaxation mechanisms (i.e. localization and decay to the substrate) and/or energy relaxation are present.²⁶

2.4.2 Dynamic Energy Relaxation

Dynamic energy relaxation of interfacial electrons has been extensively studied at thin-film dielectric/metal interfaces.⁴ Energy relaxation in solution had been studied previously using fluorescent dye molecules and excess electrons, for which theoretical models have been developed.²⁷ The time-dependent response of the

solvent coordinate to a local change in the charge distribution is termed solvation and affects reaction dynamics in solution and at interfaces.^{28, 29} The macroscopic dielectric response can be insufficient to describe the solvation response, and microscopic details of the system might need to be considered to accurately reproduce experimental results, especially at short (ps) timescales. An empirical functional form has been widely used to fit energy relaxation data in solution. The function is a sum of a half-Gaussian and multiple exponential decays.³⁰ The exponential relaxations fit the diffusional response, which results from large-scale solvent restructuring and motion, and the Gaussian component fits the inertial response from fast, small-amplitude reorientations. The timescales for energy relaxation in solution range from femtoseconds to nanoseconds.

Research on solvation in polar, bulk liquids has guided the interpretation of solvation by dielectric thin films adsorbed on metal substrates. However, differences between thin film interfaces and bulk liquids restrict quantitative comparisons. Studies of interfacial thin films typically investigate coverages under 20 Å thick in the surface normal direction, and electronic intermediate states are essentially two-dimensional. Also, the growth of stable thin films from polar solvents in UHV conditions requires temperatures 100 – 250 K below solvent freezing points. Both considerations complicate comparisons of solvation dynamics between environments.

Solvation by thin films has been observed in 2PPE measurements as a dynamic shift in electron kinetic energy. The lack of electronic degrees of freedom for electrons in IPS's implies that a dynamic kinetic energy shift must result from interactions with the surrounding environment. One method of interaction with the

environment is that of solvation by the thin film. Solvation manifests itself as a dynamic, local workfunction shift, which reduces the energy of the intermediate state electron.^{30, 31} Consequently, the IPS proves a useful probe of the layer's time-dependent dielectric response.

The energy relaxation of IPS's due to solvation at thin film interfaces has been described with a variety of functional forms including Gaussian, exponential and linear components and is highly material specific.⁴ Surface roughness of the thin film, polarity and dipole density have been shown to affect the solvation response, and solvation has been observed in nitriles, alcohols, alkanes and other systems.⁴

Observation of solvation with 2PPE is commonly conducted by acquiring kinetic energy spectra at a range of pump-probe delay times and a fixed substrate-to-detector collection angle, as depicted in Figure 2.2. The collection angle determines specific combinations of k_{\parallel} and E_{kin} which reach the detector to form the kinetic energy spectrum. The acceptance conditions are illustrated by the shaded slice in Figure 2.6. *At a fixed angle*, any dynamic energy relaxation (ΔE_{kin}) is accompanied by a shift in the parallel momentum of the electrons which reach the detector (Δk_{\parallel}). These shifts can be significant in typical systems. Solvation with a magnitude of 0.2 eV observed with electrons of an initial kinetic energy of 1 eV is common for thin films of small, polar solvents.³² This kinetic energy shift results in a corresponding 20% decrease in *observed* k_{\parallel} . Consequently, it is impossible to collect, for example, population decay dynamics of electrons with a specific k_{\parallel} at a fixed, nonzero collection angle *when moderate to large solvation is present*. Fixed- k_{\parallel} population

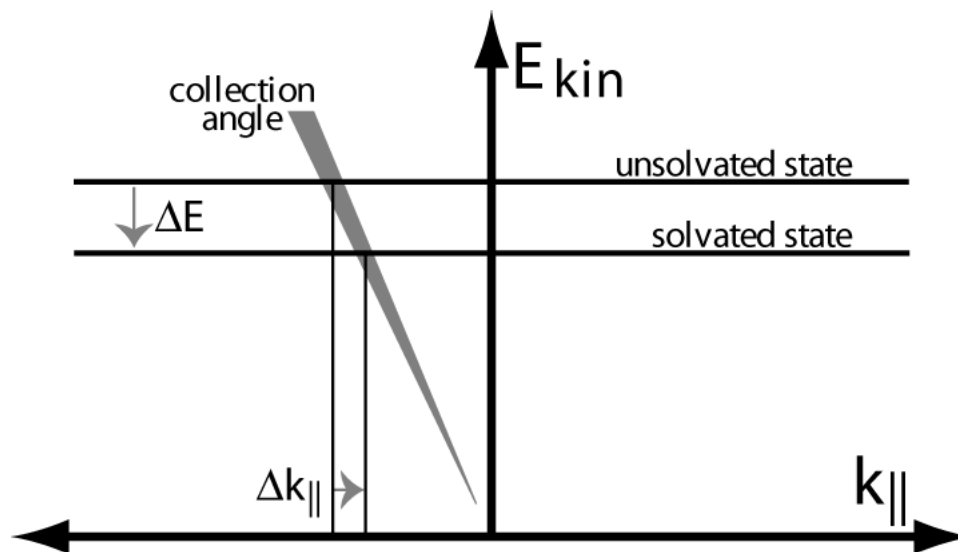


Figure 2.6: The kinetic energy (E_{kin}) of a nondispersive state is illustrated as a function of parallel momentum ($k_{||}$) before and after energy relaxation. The sample orientation with respect to the detector determines the combinations of $k_{||}$ and E_{kin} which are collected. A nonzero collection angle is displayed by the grey swath. For a fixed, nonzero collection angle, any energy relaxation causes a shift in the *observed* parallel momentum.

decay dynamics would require a prior knowledge of the time-dependent energy relaxation and readjustment of the collection angle at every pump-probe delay to compensate for the shift, a process which would prohibitively increase data collection time. A method to extract k -space dynamics from dynamics collected at multiple, fixed collection angles has not been directly proposed in the literature. However, simulations have been used to reproduce fixed-collection-angle dynamics from which k -space dynamics can be extracted.²⁰ However, the accuracy of the predictions is necessarily limited by the accuracy of the simulation assumptions.

2.4.3 Dynamic Localization

Interfacial electron localization is of fundamental interest in a variety of contexts and has consequently been well studied in UHV-grown thin films.^{19, 20, 33-35} Electron localization is the first step in charge injection into a range of semiconductor devices,³⁶ and it is also a process important to reduction at the electrochemical interface.³⁷ In angle-resolved 2PPE measurements, electron localization is observed as a dynamic shift in the effective mass of an intermediate electronic state.

The energy of a nearly free electron is lower than that of a localized electron. Dynamic localization from an initially delocalized state is not energetically favorable. Formation of a stable, localized electronic state must be accompanied by an interaction with the environment that lowers the energy of the localized state with respect to the delocalized state to overcome the energy cost of localization. As a result, localization, and the timescale on which it occurs, is sensitive to the composition, structure and

dimensionality of the surrounding environment. At thin film interfaces, energetic stabilization can be provided by static traps or through dynamic self-trapping.⁴

Static energy traps have a range of sources. Substrate roughness and low symmetry metal surfaces (i.e. Cu(775)) have been observed to cause localization of electrons.³⁸ The source of static traps can also result from the thin film. In a monolayer of buckminsterfullerene (C_{60}) deposited on Cu(111), the charge transfer to the layer is large, and the energy landscape is sufficiently corrugated to energetically favor localization of image potential state electrons.¹⁹ The previously mentioned traps are periodic or crystalline in nature, but static traps can also occur at defects. Defects can arise in amorphous thin film coverages, where the random alignment of molecules and molecular dipoles can create a rough potential landscape for electrons.³⁹

In addition to static traps, interaction between the thin film and the electron can dynamically induce the formation of trap sites, referred to as self-trapping.⁴⁰ In systems with moderate to large solvation, concurrent localization is to be expected. The localization of charge density around a few molecules in the thin film enables maximal interaction and energy stabilization between the electron and the thin film.

The primarily two-dimensional character of thin film interfaces can affect localization behavior, as seen in a NaCl bilayer deposited on the Cu(111) surface. Conduction band electrons are conclusively shown to reside in the NaCl layer and to dynamically localize.⁴¹ The localization is attributed to small polaron formation. The localization phenomenon is quite unusual, as electron localization is not present in bulk NaCl crystals. Previous studies have indicated the increased deformability of thin films with respect to the bulk crystal.⁴² Both the increased deformability and the

reduction of the band width in NaCl thin films are proposed as caused for the small polaron formation in thin films that is absent in bulk NaCl. The study serves to underscore the important differences between interfacial and bulk processes, which results from the reduced dimensionality.

A localized electronic state appears as a nondispersive feature in 2PPE experiments. Because electrons are excited from delocalized, valence band electronic states, intermediate state electrons are expected to be initially delocalized. Nondispersive features observed at instantaneous pump-probe time delays are interpreted as dynamically localizing on a timescale faster than the instrument response.⁴ The timescale for this localization implies a lack of dynamic interaction with the surface nuclear coordinates and restricts the formation of a localized state to interactions with static trap states already present at the interface prior to electron excitation. Hence, electrons observed in initially localized states are referred to as *statically localized*.

A dynamically-localized electronic state is not observed at instantaneous pump-probe delay times. The populations of nondispersive features corresponding to dynamically-localized electronic states grow in as a function of pump-probe delay time with rise times of tens to hundreds of femtoseconds. Dynamic localization from an initially delocalized state can arise from dynamic self-trapping, migration to static traps or a combination of both mechanisms. The mechanism of localization might be accessible if the localization rate were known as function of delocalized state parallel momentum. However, the separation of 1) intraband relaxation within the delocalized state, 2) momentum-dependent interband relaxation to the localized state and 3) decay

to the substrate has proven to be a challenging problem and remains unsolved.²⁶

Regardless of mechanism, dynamic localization is observed in a number of systems, and it remains of fundamental interest as a first step in charge injection.

2.5 Conclusion

Physical processes occurring at the interface are often quite different than the behavior in bulk. Intermediate electronic states, in particular image potential states, are quite sensitive to the environment at the interface. Two-photon photoemission provides a method to populate intermediate states and observe their dynamic evolution. The interconnected dynamics of the dispersion, population and energy of interfacial electrons in thin film interfaces yield a great deal of insight into the physics occurring at interfaces. The UHV, angle-resolved 2PPE technique is quite versatile and can investigate these dynamic properties for a wide array of interfacial systems.

Chapter 3: Experimental Apparatus

3.1 Overview

Ultrathin film growth and characterization requires a number of specialized techniques and methods. While the experimental apparatus has been discussed in detail by other sources,^{14, 17, 43} some aspects pertain directly to the contents of this thesis. In addition, I have installed and modified chamber components to extend measurement capabilities. Other aspects of the apparatus, which affect data collection and interpretation, have only recently become fully understood and are discussed.

3.2 Ultrathin Film Deposition

Exposure of the Ag(111) substrate to a flux of molecules can result in reproducible ultrathin film growth when the substrate temperature is sufficiently low to permit molecular adsorption. The selection of method, by which the flux of molecules is generated, depends on the vapor pressure of the desired adsorbate. Two methods of flux generation are available in the current experimental system.

The first method, sample line dosing, is ideal for substances with a high room-temperature vapor pressure (≥ 1 torr). First, the substance of interest (adsorbate) is transferred to a glass bulb in a nitrogen environment and attached to a high vacuum line ($\sim 5 \times 10^{-7}$ torr). Freeze-pump-thaw cycles can be performed to remove residual

impurities from the adsorbate, and adsorbate purity can be verified by a quadrupole mass spectrometer in the main UHV chamber (Section 3.3). The vacuum line is filled with the vapor pressure above the adsorbate in the bulb. The main UHV chamber, containing the Ag(111) crystal, is backfilled from the vacuum line via a variable leak valve. By recording the main chamber pressure and exposure times, dosing can be recorded in units of Langmuir ($1 \text{ Langmuir} \equiv 1 \text{ } \mu\text{torr} \times 1 \text{ s}$).

The second method, epitaxial dosing, is ideal for samples with both low room-temperature vapor pressures (μtorr or less) and substantial vapor pressures (10^{-4} torr) when heated. A crucible containing the sample is loaded into an effusion cell, described elsewhere,⁴³ which is subsequently evacuated to 10^{-7} to 10^{-9} torr. Heating of the crucible provides the vapor pressure necessary to establish a flux of molecules. A line-of-sight path is established to the sample via removal of a shutter, by which dosing can be regulated. Flux can be adjusted by varying the crucible temperature up to a maximum of 1500 K.

Notable limitations are placed on sample selection by constraints of current dosing methods. An intermediate range of room-temperature vapor pressures exists between μtorr and torr, for which no suitable dosing method is present. Dosing from the sample line can be extended to slightly lower pressures by mild heating of the glass bulb. However, both condensation in the sample line and preferential vaporization of impurities are likely. These effects firmly limit sample vapor pressure to a minimum of mtorr, and reproducible dosing of a pure sample becomes *extremely* difficult at sample line pressures as high as 450 mtorr. Epitaxial dosing can be extended to samples with slightly higher pressures ($\sim 10^{-4}$ torr), but samples

completely sublime from the crucible in a day or less. The time constraint precludes a bakeout of the effusion cell, which increases the partial pressure of impurities within the cell. The rapid sublimation of sample and lack of a bakeout affect the reproducibility and purity of epitaxially grown layers in this pressure range.

Additionally, not all low room-temperature vapor pressure materials are suitable for epitaxial dosing. The temperature, at which samples decompose, sets an upper limit on crucible heating. Many materials do not have sufficient vapor pressures for epitaxial dosing at any temperature below the onset of decomposition. Finally, materials which decompose upon exposure to air can only be dosed via the sample line. No method or simple upgrade exists to load materials into the effusion cell while constantly in an inert atmosphere.

3.3 Mass Spectrometer

3.3.1 Default Specifications

The mass spectrometer was replaced during my graduate work. The replacement marked a major upgrade in our sample analysis capability and facilitated the conduction of thermal desorption spectroscopy experiments (Chapter 5). The selection of a mass-to-charge ratio to observe was a manually accomplished process with the old mass spectrometer, which took ~1 second. Data logging was also manually accomplished. Finally, the unit could not be interfaced with a modern computer for data logging, automated control, or the synchronization of data logging

with other measurements. Acquisition of a full mass fragmentation spectrum was time consuming and tedious.

The new mass spectrometer is a Stanford Research Systems Residual Gas Analyzer 300 (SRS RGA 300). It utilizes a quadrupole mass filter to select mass-to-charge ratios to monitor. The RGA 300 is controlled by Windows or Labview software packages provided by SRS. Data logging is also performed by the software. Acquisition of a low-noise mass fragmentation pattern takes on the order of 15 s. The data sampling rate for acquisition of a specific mass-to-charge ratio is ~100 ms. The speed of acquisition greatly simplifies an evaluation of the cleanliness of the main chamber and adsorbates from the sample line.

3.3.2 Modifications for Thermal Desorption Spectroscopy

Thermal desorption experiments require the detection of small amounts of material. To achieve adequate sensitivity for sub-monolayer resolution, the mass spectrometer must be in within millimeters of the sample. The default configuration of the RGA 300 allows for a chamber penetration depth of ~3.75 cm. The manipulator arm on which the Ag substrate is mounted is incapable of placing the substrate near the mass spectrometer. A standard modification, detailed in the RGA 300 Operating Manual, was employed to achieve a maximum penetration of 17 cm and allow for thermal desorption measurements. The modification is illustrated in Figure 3.1. The quadrupole Cover Nipple is removed from assembly, which allows the 2.75 in CF flange further from the ionization tip to be attached to vacuum chamber. The

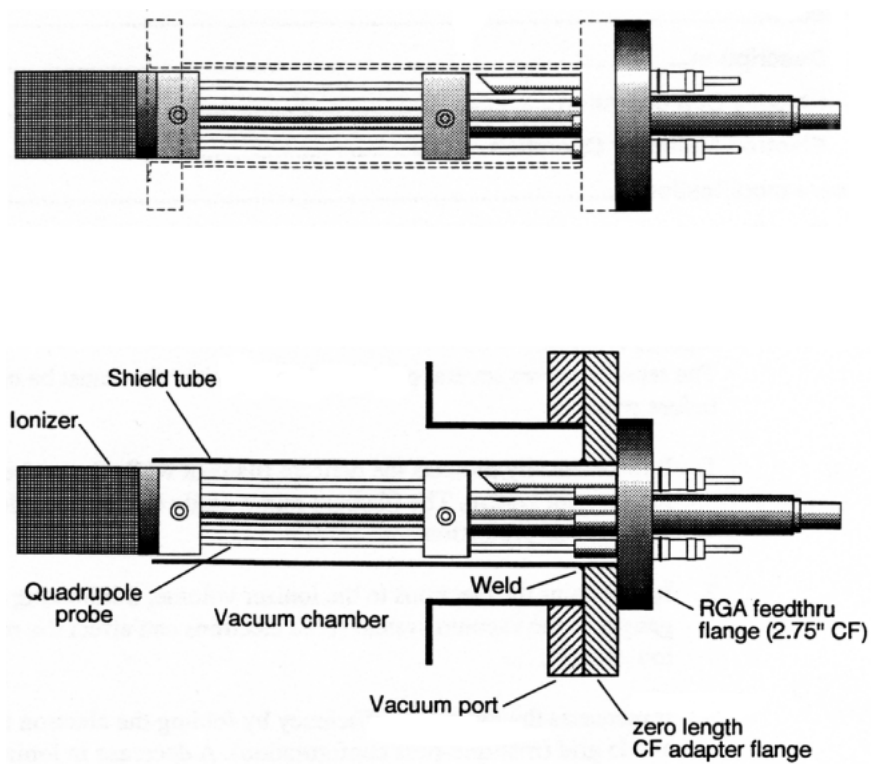


Figure 3.1: The quadrupole mass spectrometer is shown in its default configuration (top) and after modification (bottom). The Cover Nipple (dotted) has been removed and replaced with the shield tube

quadrupole control electronics are initially calibrated in the presence of the Cover Nipple, which contributes to the overall capacitance of the system. Therefore, a 1/8 in thick, steel type 316 shield tube is used to substitute for the capacitive effects of the Cover Nipple. The shield tube was welded to a zero-length adapter by the UC Berkeley Chemistry Department machine shop. After the modification, the ionization tip is unfortunately still located several centimeters from the Ag substrate. A decreased tip-to-substrate distance for additional sensitivity could only be achieved with the purchase of a new mass spectrometer or substrate manipulator arm.

Initial desorption experiments indicated that molecules desorbing from the sample mount contributed significantly to the observed signal and could obscure desorption from the Ag(111) surface. A standard solution, the Feulner cup, has been reported in the literature, which surrounds the ionization tip.⁴⁴ The cup serves as an aperture which blocks contributions from the sample mount when placed in front of the Ag crystal. Ideally, the cup should be constructed from a chemically inert material such as glass, so that molecules that collide with the cup interior wall prior to ionization do not react. However, the charging of a glass surface within the UHV chamber would prohibit reproducible photoemission measurements. Therefore, steel type 316 was also used for the Feulner cup. The cup is secured to the shield tube by three set screws. Both the sample mount and Feulner cup are illustrated in Figure 3.2 and Figure 3.3. A snug fit between cup and shield tube was ensured by simultaneous construction of both components.

The flux of molecules through the aperture during desorption creates an elevated local pressure of fragmented products within the Feulner cup and shield tube

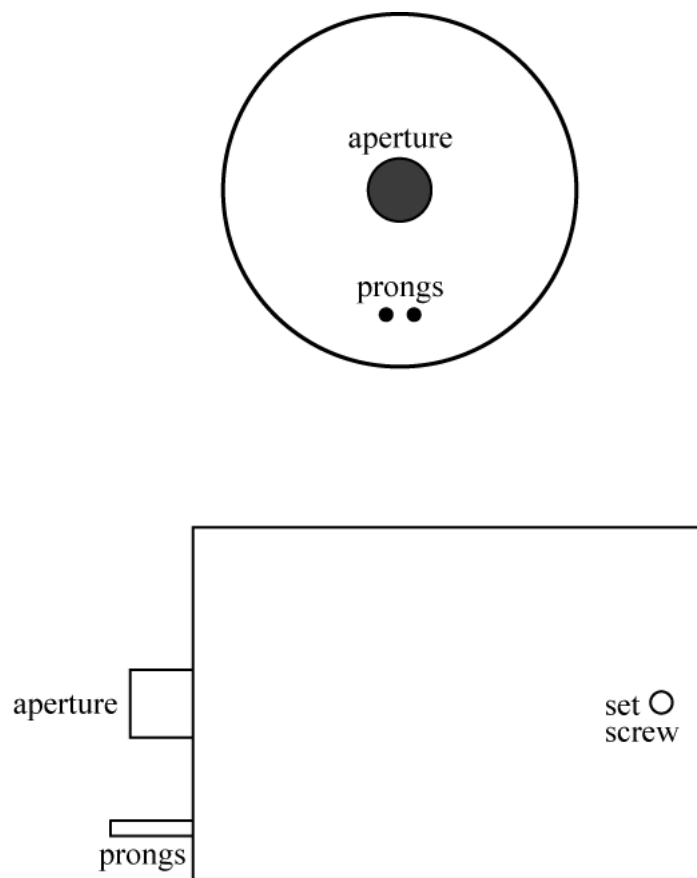


Figure 3.2: Front (top) and side (bottom) views of the Feulner cup are diagrammed. The cup itself is hollow and constructed from $1/8^{\text{th}}$ in steel.

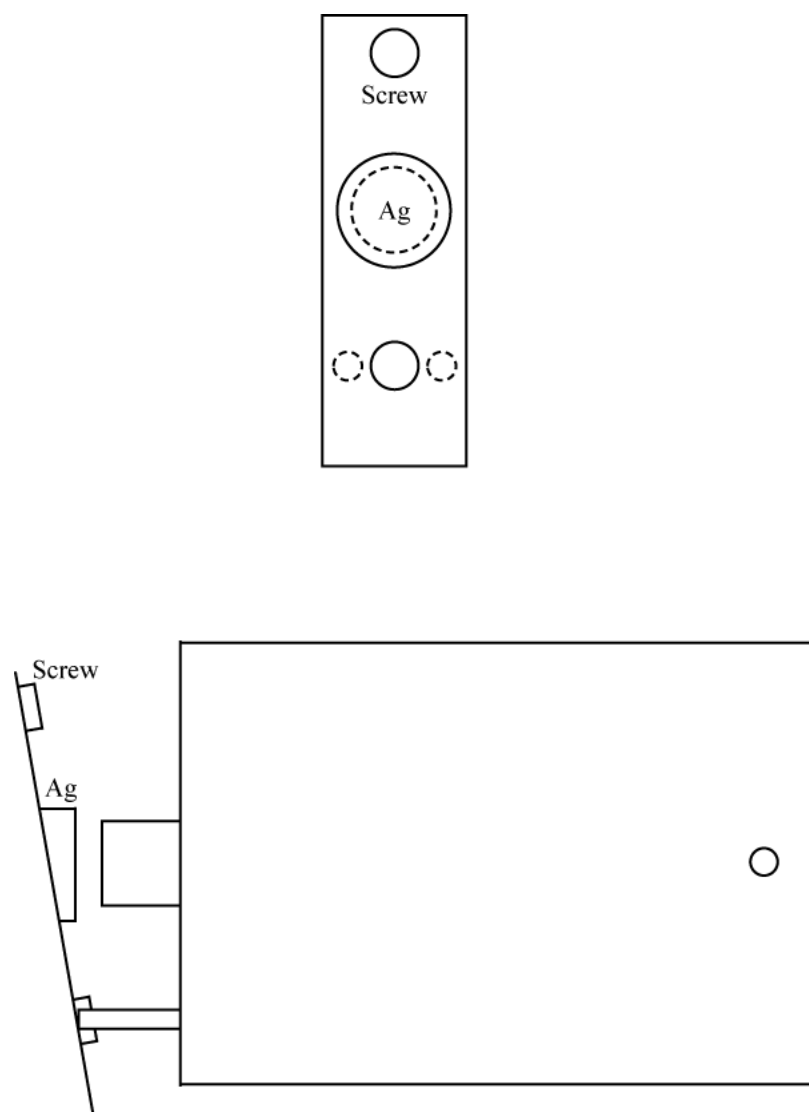


Figure 3.3: The sample plate is shown in relation to the Feulner cup from a front (top) and side (bottom) view. The location of the aperture and prongs are represented by the dotted lines in the upper panel. A minimum separation is created between the aperture and crystal by the prongs, as shown in the lower panel. The sample clips and cooling block have been omitted for clarity.

assembly. Without additional venting channels, the only pressure release is *back* through the Feulner cup aperture. Backflow of fragmented molecules would interfere with and unnecessarily broaden desorption peaks. Three vents were added to base of the shield tube at the time of Feulner cup installation to provide additional pressure release channels. The vents are bored in the shield tube over the ion detection portion of the mass spectrometer to minimize changes to the capacitive environment near the quadrupole.

The function of the Feulner cup prongs is illustrated in Figure 3.3. The prongs were designed in response to concerns that the Ag crystal might incur damage if it were to scrape the Feulner cup from human error in sample positioning. The safety prongs ensure a minimum separation between the crystal and the aperture. Ideally, the prongs would have been located above the aperture. The configuration would allow for quick, visual alignment of the substrate with respect to the aperture by symmetrically centering the prongs around the upper sample mount screw. However, the typical repositioning of the sample manipulator arm involves the raising of the crystal with respect to the Feulner cup (in the coordinate system of Figure 3.3). Safety prongs positioned above the sample would therefore represent a significant crystal scraping hazard in the event of an errant realignment, while safety prongs positioned below the sample pose relatively little risk as a function of user error. In response to this risk, the safety prongs are located below the aperture.

Initial determination of manipulator arm settings was achieved during installation when the chamber was at atmospheric pressure. The zero-length adapter with the shield tube and attached Feulner cup was installed prior to the insertion of the

mass spectrometer. By centering an eye with respect to the zero-length adapter hole, the correct horizontal and vertical position of the crystal could be established with respect to the aperture. The crystal tilt angles were established by utilizing the reflection off of the Ag crystal.

3.4 Substrate Temperature Control

The method of Ag substrate temperature control was modified during my graduate work. A thermocouple in contact with the substrate monitors its temperature, and a resistive heating element underneath the sample elevates sample temperature from room-temperature or from a cryogenically cooled base temperature. These components are described in detail elsewhere and have not been modified.¹⁷

The old method of temperature control utilized an Eurotherm 815 Programmer/Controller. The Eurotherm 815 was a stand-alone unit that accepted K Type thermocouple input from the substrate thermocouple. An internal algorithm determined an appropriate output voltage. The output drove a Kepco variable power supply, which output power to the resistive heating element under the sample. The signaling and feedback process is illustrated in Figure 3.4.

The new method of temperature control is to replace the Eurotherm 815 with a custom PID control algorithm run from a personal computer. The design theory of the PID algorithm is discussed extensively in Chapter 5. In the new configuration, the thermocouple output is connected to a National Instruments SC-2345 Signal Conditioning unit configured for K Type thermocouple input. Software provided with

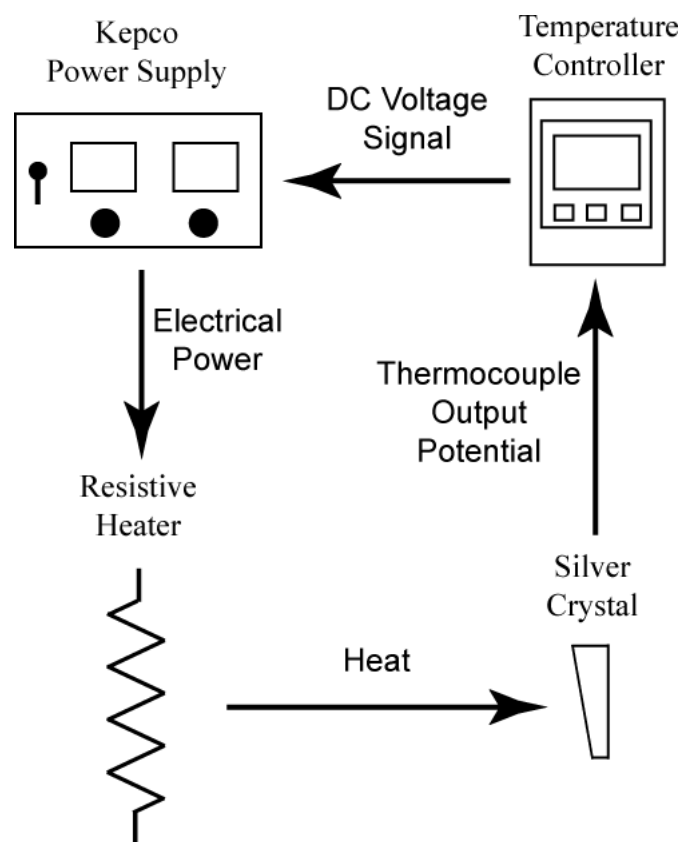


Figure 3.4: The input and output of temperature control components are represented by the labeled arrows. The component labeled temperature controller had been the Eurotherm 815, but was replaced with a National Instruments Signal Conditioner connected to a PC.

the SC-2345, written in Labview, provides the low-level functionality for execution of basic tasks from a personal computer: reading the thermocouple contact potential from the unit and outputting a voltage from the unit. Thus, the SC unit provides the same input and output as the Eurotherm 815.

The replacement of the Eurotherm 815 with the PC-driven SC-2345 allows for easy data logging of temperature as a function of time, which can be synchronized to other PC-controlled instruments. Additionally, temperature control programs and algorithms are more accessible and customizable via coding of Labview programs. However, the replacement of the Eurotherm 815 is not without drawbacks, as the increased flexibility of a PC is accompanied by increased complexity. A PC is much more prone to system crashes, driver compatibility issues and operating system or software upgrade incompatibility issues, which represent non-trivial concerns. The Eurotherm, in contrast, functioned as a reliable black box.

3.5 Ultrafast Laser System

The laser system used to collect 2PPE data has been described in detail elsewhere.¹⁵ The relevant features are a laser that generates <100 fs FWHM pulses at 200 – 250 kHz of tunable wavelengths from 490 – 740 nm. These pulses are frequency doubled, producing ~ 10 nJ and ~ 20 nJ pulses for the frequency double and residual fundamental wavelengths, respectively. The fundamental (vis) pulse is split from the second harmonic (UV) pulse by a dichroic mirror and delayed by a translation stage with one micron (6.7 fs) step size to provide temporal separation.

3.6 Systematic Error in 2PPE Dynamics: A Ghost Image

A systematic error was discovered in the method, by which pump-probe dynamics were collected, during my graduate work. The error produces an artifact in pump-probe dynamics, which appears as a feature with population, energy relaxation and/or localization dynamics. The artifact affects the interpretation of dynamics collected prior to the discovery. All data presented in this work was either collected or reproduced after implementing corrections for the systematic error. Evidence of the artifact can be found in dynamics dating back to the year 2000, and dynamics published in a journal article contain the artificial feature.

3.6.1 History of Symptoms

The history of the symptoms leading to the eventual diagnosis of the systematic error is briefly outlined. It is hoped that a critical discussion of the diagnostic process will 1) aid in the interpretation of previously collected data, 2) aid in the detection of the error, should it arise again, and 3) most importantly, spare future researchers from wasting a great deal of time by presenting practices that are generally applicable to an analysis of data acquisition methods.

An odd phenomenon, displayed in Figure 3.5,⁴⁵ was observed in acetonitrile thin films in 2000. At time delays when nearly all photoemission signal had ceased, sudden recurrences of intensity were detected. A description of the phenomenon was

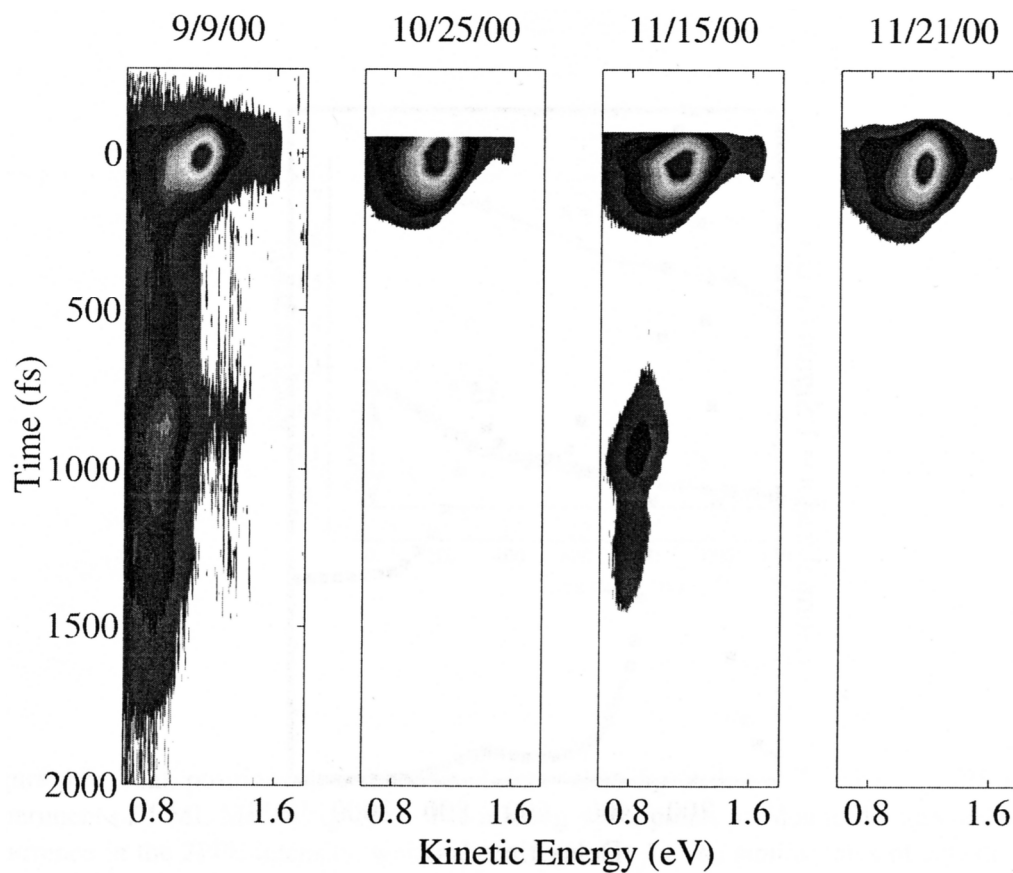


Figure 3.5: Time-resolved dynamics of acetonitrile monolayers grown on various days. Data was not collected at delays below 0 fs on some days, which appears as a sharp drop-off. The recurrence is only visible intermittently, despite similar layer growth conditions.

not present in the literature. Within an experiment, the intensity profile was quite reproducible and not due to fluctuations in laser intensity. However, as evidenced by Figure 3.5, the same dosing procedure, repeated on multiple days, failed to reliably reproduce the long-time recurrences.

A small air leak was detected in the sample line via mass spectroscopic analysis in 2002. It was hypothesized that the leak introduced contaminants which were co-dosed into ultrathin films. Water represented the atmospheric component most likely to co-adsorb with small, polar alcohols and nitriles. The source of the recurrences was tentatively assigned to water contamination. While the assignment of a mechanism for population recurrence was impeded by the scarcity of mixed-component thin film studies, the theory of inadvertent contamination satisfactorily explained the day-to-day irreproducibility of the recurrence. It was at this point that I began research in the Harris lab.

An accurate characterization of the relative concentrations and locations of components within a mixed-component thin film was necessary for a scientific investigation of recurrences. This phenomenon provided the impetus and personal motivation to add thermal desorption spectroscopy functionality to the UHV chamber. Mixed alcohol/water thin films were grown and characterized by 2PPE and thermal desorption spectroscopy. While I could easily produce recurrences in mixed thin films, an extensive range of experiments showed no dependence of the recurrence on the water concentration in the thin film. The results motivated a long-time dynamics scan of clean Ag, in which the presence of the recurrence was detected on a verifiably pristine Ag(111) surface. The results of one such scan are presented in Figure 3.6.

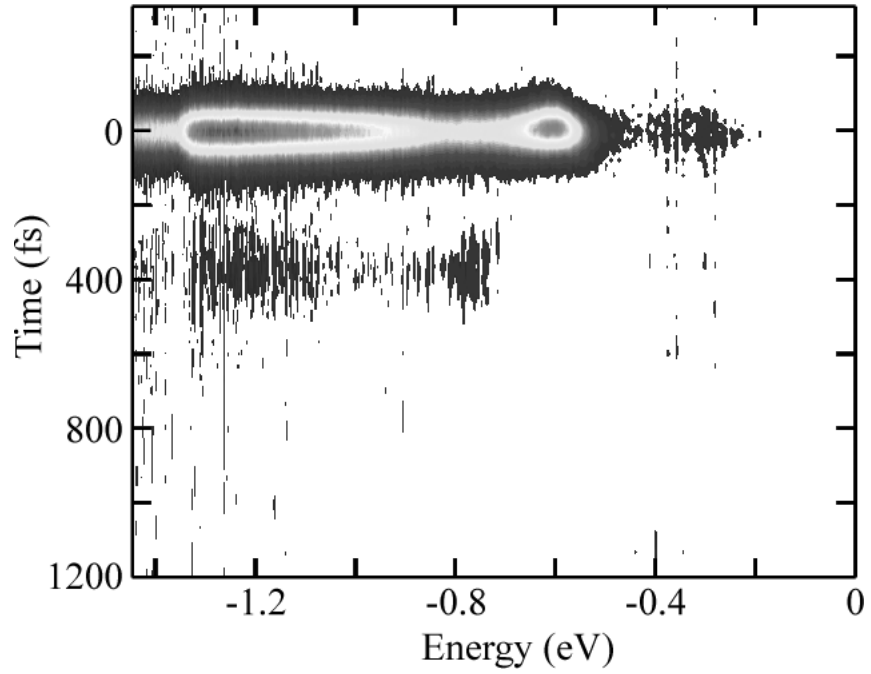


Figure 3.6: A dynamics scan of the clean Ag surface using a probe wavelength of 705 nm and collected at a grid bias 0.56 V more positive than the correct clean Ag grid bias. The surface state is visible at -0.4 eV, and inelastic scattering is visible at lower energies. A ghost of the primary image is seen at 400 fs which captures both the surface state and inelastic scatter features.

The dynamics of electrons at bare metal surfaces were well-known, and no mechanism could plausibly explain the recurrence phenomenon at the clean Ag(111) interface. I concluded a systematic error must be the source of recurrences.

3.6.2 The Probe Pre-pulse and the Ghost Phenomenon

A low-intensity femtosecond pulse of light centered around a wavelength of 800 nm was subsequently discovered to temporally precede the probe pulse by 500 fs to 800 fs. The pre-pulse originated from the unconverted residual intensity of the 800 nm input pulse that powered the optical parametric amplifier (OPA). The temporal delay of the main probe pulse resulted from the positive chirp of optical components within the amplifier. The complete profile of the pulse exiting the amplifier in frequency and time is illustrated in Figure 3.7.

The perturbation imposed on dynamics scans by this unusual pulse profile is highly analogous to the phenomenon of ‘ghosting’ in analog television sets. When a portion of a transmitted RF television signal travels a longer path to the receiving antenna after reflection from a large stationary object or land feature, a faint, horizontally-shifted, superimposed duplicate of the primary screen image is seen. The phenomenon presumably takes its name from the resemblance of semi-translucent television images of human forms, resulting from the delayed signal, to the conventional description of ghosts in fiction. It is important to note that, except for the temporal and intensity offsets, the ghost image is identical to the primary image. The same observation is true for 2PPE dynamics: the temporally-offset, less-intense,

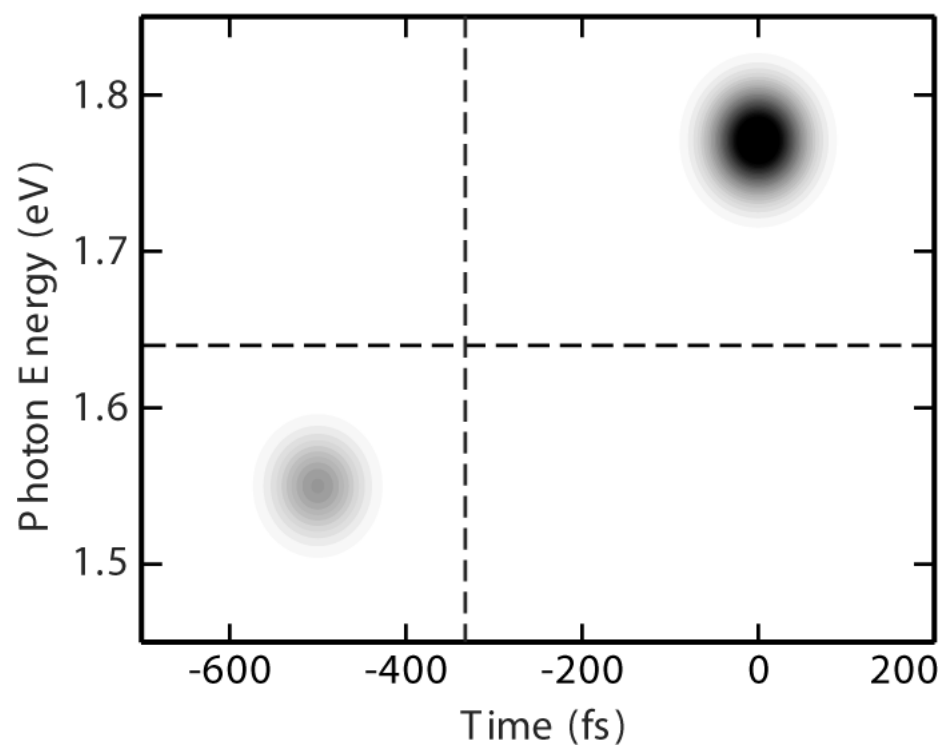


Figure 3.7: The pulse profile in energy and time is illustrated. Intensity is indicated by the shading. The dotted lines denote the lower limits to which the pulse is characterized on a daily basis.

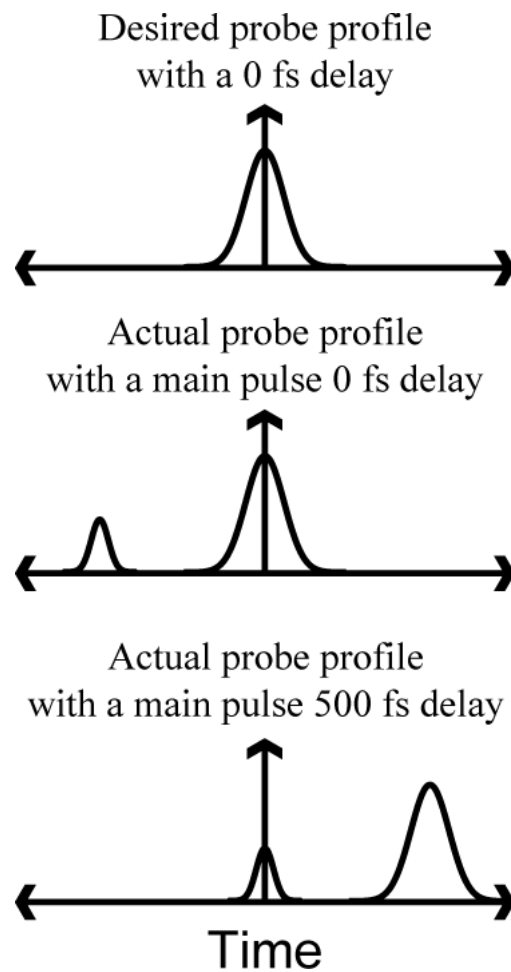


Figure 3.8: The probe pulse intensity is displayed as a function of time. The time axis is defined such that a time of 0 corresponds to temporal overlap with the pump pulse (not shown), and positive time corresponds to a probe delayed with respect to the pump. At a large enough positive delay, the pre-pulse is temporally overlapped with the pump pulse.

superimposed, ghost 2PPE dynamics resulting from the pre-pulse exhibit the same peak widths and population, energy relaxation and localization dynamics as the dynamics resulting from primary probe pulse.

The mechanism, by which a pulse *preceding* the primary probe pulse generates signal at time delays *following* pump-probe overlap, is not immediately intuitive. Figure 3.8 illustrates the circumstance. The time axis reported in a 2PPE dynamics scan is the delay between the pump and primary probe pulses. The axis is referenced to the time delay of temporal pump-probe overlap, set as $t = 0$. At a primary probe pulse delay of 0 fs, the probe pre-pulse arrives at a delay of -500 fs. When the primary probe pulse is moved to a delay of +500 fs, the pre-pulse arrives coincident with the pump and generates 2PPE electrons. Thus, photoemission signal is detected at a delay of +500 fs, but it must be remembered that the time delay references the primary pulse, not the pre-pulse. Consequently, pre-pulses produce photoemission signal at positive pump-probe time delays.

3.6.3 Pre-Pulse Detection and Elimination

Relatively few techniques for pulse profile characterization are available or generally needed for the current experimental apparatus, and the existence of the pre-pulse remained undetected by several researchers prior to my work. Autocorrelation suffices for day-to-day dispersion compensation adjustments, and the removal of the pre-pulse does not measurably affect the autocorrelated pulse width. A visible wavelength spectrometer is used to measure the wavelength of light generated from

the optical parametric amplifier, but the collection window was rarely set to larger than 50 nm. Finally, clean Ag(111) dynamics are taken at the beginning of all experiments to verify surface cleanliness and extract a pump-probe cross-correlation width. However, the Ag(111) electron dynamics are well-known and short;¹⁷ consequently dynamic scans of the clean Ag surface rarely exceeded pump-probe delays of 300 fs. The typical day-to-day pulse characterization ranges in both frequency and time are labeled in Figure 3.7 as assessed by pump-probe dynamics and the spectrometer.

The pre-pulse was simple to remove once its existence had been discovered. A prism compressor is used to compensate for positive chirp accumulated in the optical parametric amplifier. As shown in Figure 3.9, frequencies of light are spatially dispersed within the compressor assembly. A spatial filter was subsequently inserted to block the pre-pulse at 800 nm and prevent ghosting. The spectrometer is used daily to verify that the entirety of the pre-pulse has been terminated. Alarming, the pre-pulse can constitute up to a third of total pulse power. The retroreflector in Figure 3.9 is quite small (1.26 cm) and often functions as an additional spatial filter. The day-to-day fluctuations in alignment through the compressor and sporadic termination of the 800 nm light by the retroreflector explain the day-to-day irreproducibility of ghost artifacts in dynamics.

3.6.4 Identification of Artifacts in Previously Collected Data

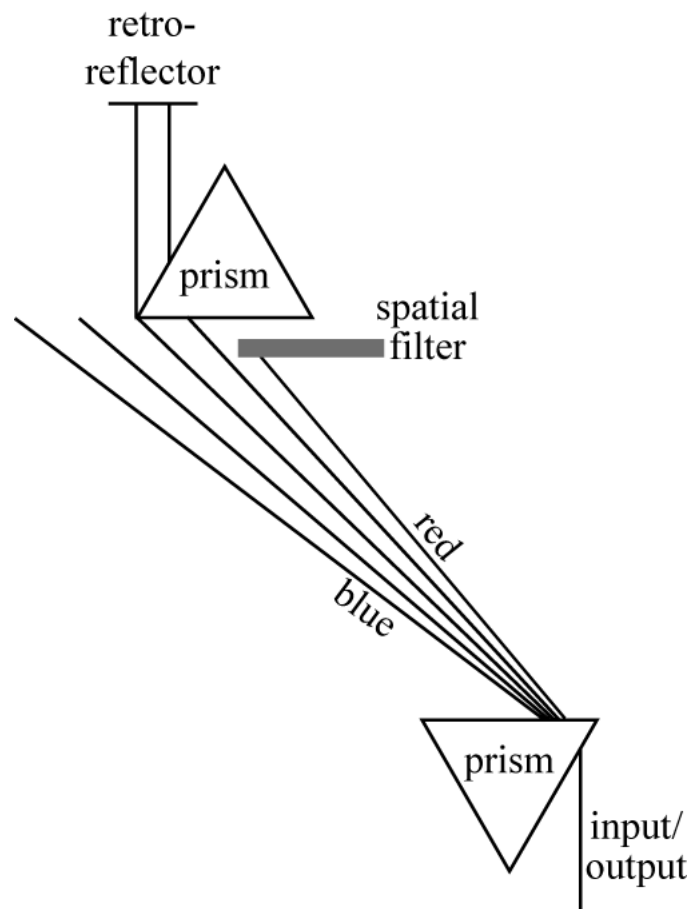


Figure 3.9: The paths of rays of various wavelengths are traced through the prism compressor. Initially, all wavelengths are collinear. Spatial dispersion allows the insertion of a spatial filter to block the reddest wavelengths.

Without interference from features generated by the primary probe pulse, ghost features can be easily identified in 2PPE dynamics. Identification of ghost features is primarily useful in the evaluation of 2PPE dynamics collected prior to discovery of the pre-pulse. The energy shift between a feature and its ghost corresponds to the energy difference between the primary probe photon energy and the energy of a photon with a wavelength of 800 nm, that is 1.55 eV. The temporal offset of ghost features is characteristically between 500 fs and 800 fs. Shorter wavelengths pass through optical components in the OPA more slowly than longer wavelengths; correspondingly, when the OPA is tuned to bluer wavelengths, the delay between the primary pulse and the pre-pulse is observed to be larger than when tuned to redder wavelengths.

Additionally, the ghost dynamics are qualitatively and quantitatively similar to primary dynamics, in analogy to ghosting in television reception. Quantitatively, the number of peaks, peak widths, population relaxation dynamics, energy relaxation dynamics and localization dynamics are the same for primary and ghost dynamics. Qualitatively, the quantitative aspects combine to create distinctively similar shapes for primary and ghost features in contour plots of 2PPE dynamics. The ease of ghost identification by shape is shown in Figure 3.10, where alcohol ultrathin film dynamics with ghost features, published in JPC B, are compared to DMSO ultrathin film dynamics without ghost features.¹³

Unfortunately, the combination of strong dynamic localization and solvation result in an energy shift and population recurrence similar to ghost dynamics. While

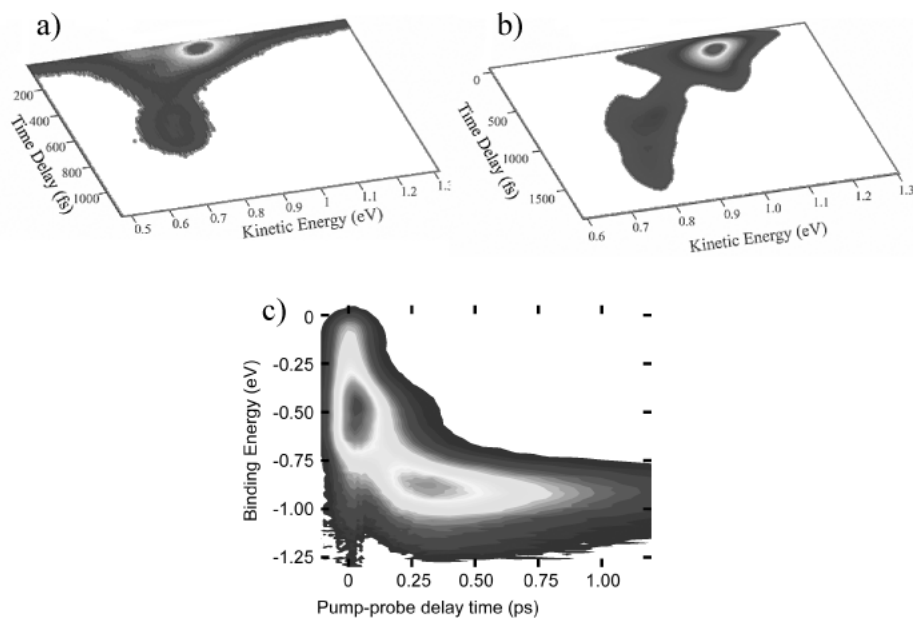


Figure 3.10: The similarity in shape of the long-time feature with respect to the primary feature is evident in panels a) and b). The long-time feature in panel c) is quite different from its primary feature. Panels a), b) and c) are a >ML coverage of methanol, a >ML coverage of butanol, and 2 ML of DMSO, respectively.

the quantitative and qualitative criteria can eliminate ghosting as the *sole* source of dynamics in these systems, the only way to ascertain that ghosting does not contribute to dynamics in these systems is to repeat the experiments with the pre-pulse blocked. For instance, the entirety of data collected in Chapter 4 was retaken after discovery of the pre-pulse to eliminate the potential contribution of ghosting.

3.6.5 General Application to Data Collection Methodology

The preceding discussion would be somewhat remiss without a reflection on generalized, scientific practices which could have been used to more quickly identify the collection of erroneous data. When an observable exhibits such unusual behavior that further study is merited, it is useful to first rigorously verify correct instrumental function. An invaluable tool to troubleshoot an experimental technique, which was in this case neglected for years by many researchers, is the study of a well-characterized reference sample *under the relevant experimental conditions!* In the present case, 2PPE dynamics were taken on a regular basis on such a reference material, the clean Ag(111) surface. However, the reference material dynamics were never extended to pump-probe delay times relevant to the phenomenon of interest, i.e. recurrences on the > 500 fs timescale. Dozens, if not hundreds, of experiments were conducted to investigate the nature of recurrences by multiple researchers, and at the beginning of every experiment, the explanation for the phenomenon lay 200 fs further in time than our characterization of our reference material. In short, infinitesimal lapses of

scientific rigor can result in dramatic misinterpretations of results, and the *proper* use of a reference material is an invaluable tool.

Chapter 4: The Ultrafast Dynamics of Image Potential State Electrons at the Dimethylsulfoxide/Ag(111) Interface

4.1 Introduction

In electrochemically relevant systems, interfacial capacitance affects signal collection and heterogeneous charge transfer.⁴⁶⁻⁴⁸ Charge accumulation at the contact surface occurs when materials of dissimilar chemical potentials and/or applied voltage biases are unable to attain electronic equilibrium through interfacial charge transfer (i.e. conduction or faradaic current). Charge is stored by an electrolyte concentration gradient and dielectric solvent reorganization on the solution side of the interface and by electron accumulation at the electrode surface. This system is commonly referred to as the electrochemical double layer. The charge storage properties of the double layer can be described as capacitor-like in nature, with the notable deviation from a classical capacitor being the potential-dependent capacitance. A standard definition describing double layer capacitance is the differential capacitance (C_d) and is given in Equation 4.1 in terms of the surface charge (Q) and applied potential (V).⁴⁹

$$C_d(V) = \frac{\partial Q}{\partial V} \quad (4.1)$$

Several models of the electrochemical double layer, including the Helmholtz, Gouy-Chapman, Gouy-Chapman-Stern and jellium descriptions have been used to varying degrees of success in the study of interfacial capacitance, spanning over a century of research.⁵⁰⁻⁵⁴

Dimethylsulfoxide (DMSO), a common electrochemical solvent, exhibits an uncharacteristically low differential capacitance at noble metal electrodes (7-10 $\mu\text{F}/\text{cm}^2$ over a 1.5 V range including the potential of zero charge). Similar, polar, high-dielectric constant electrochemical solvents can show differential capacitances much higher (50 $\mu\text{F}/\text{cm}^2$ for acetonitrile under identical experimental conditions).⁵⁵ DMSO interacts chemisorptively with noble metal surfaces.⁵⁵ Both the oxygen and sulfur sites interact strongly with the metal to cause displacement of electrolytes and other solvents from the surface in solution. Hindered rotation of the DMSO dipole has been proposed to reduce the interfacial DMSO response to potential changes and lower its interfacial capacitance,^{55, 56} in accordance with established double layer theory.⁵⁷ As we will demonstrate, this mechanism can be directly tested by comparing the dielectric response of the chemisorptive monolayer with that of various multilayer coverages using two-photon photoemission in an ultra-high vacuum environment.

Ultra-high vacuum (UHV) thin-film interfaces have been used to simulate the electrochemical double layer for decades.⁵⁸ This formulation allows interfacial characterization methods to be employed that are incompatible with immersed electrode systems. Several UHV techniques can provide valuable energetic and structural information to complement immersed electrode results. However, vastly different conditions in the immersed electrode and UHV environments, including disparate temperature ranges and variations in surface morphology, can make extraction of relevant data difficult.⁵⁹ Despite these limitations, numerous studies have shown relevance of electrochemical information accessible from UHV interfaces.^{60, 61}

4.2 Experimental

Sigma-Aldrich anhydrous grade DMSO ($\geq 99.9\%$ DMSO, $\leq 0.005\%$ water) was transferred to a glass bulb in a nitrogen environment and attached to a high vacuum line ($\sim 5 \times 10^{-7}$ torr). Multiple freeze-pump-thaw cycles were performed to remove residual impurities, and DMSO purity was verified by a quadrupole mass spectrometer in the main UHV chamber. The main UHV chamber containing the Ag(111) crystal was backfilled with DMSO from the vacuum line via a variable leak valve. Main chamber pressure and exposure times were recorded, and dosing is reported in units of Langmuir ($1 \text{ Langmuir} \equiv 1 \text{ } \mu\text{torr} \times 1 \text{ s}$). All reported ultrathin films were dosed at an uncorrected pressure of 3.5×10^{-8} torr. Substrate temperatures of 210 K and 200 K were used for monolayer and thicker coverage growth, respectively.

The Ag(111) single crystal was prepared prior to DMSO exposure with Ar^+ ion sputtering (500 K, 500 eV, 5×10^{-5} torr) followed by annealing at 725 K in an UHV environment. Surface quality and purity could be verified by LEED and Auger spectroscopy as well as 2PPE dynamics scans.

A background spectrum was acquired at 3.3 ps and subtracted from all time-dependent spectra to remove single pulse photoemission mechanisms (i.e. UV-UV, vis-vis-vis). 2PPE spectra were collected with wavelengths 720 nm or longer to avoid significant one-photon photoemission.

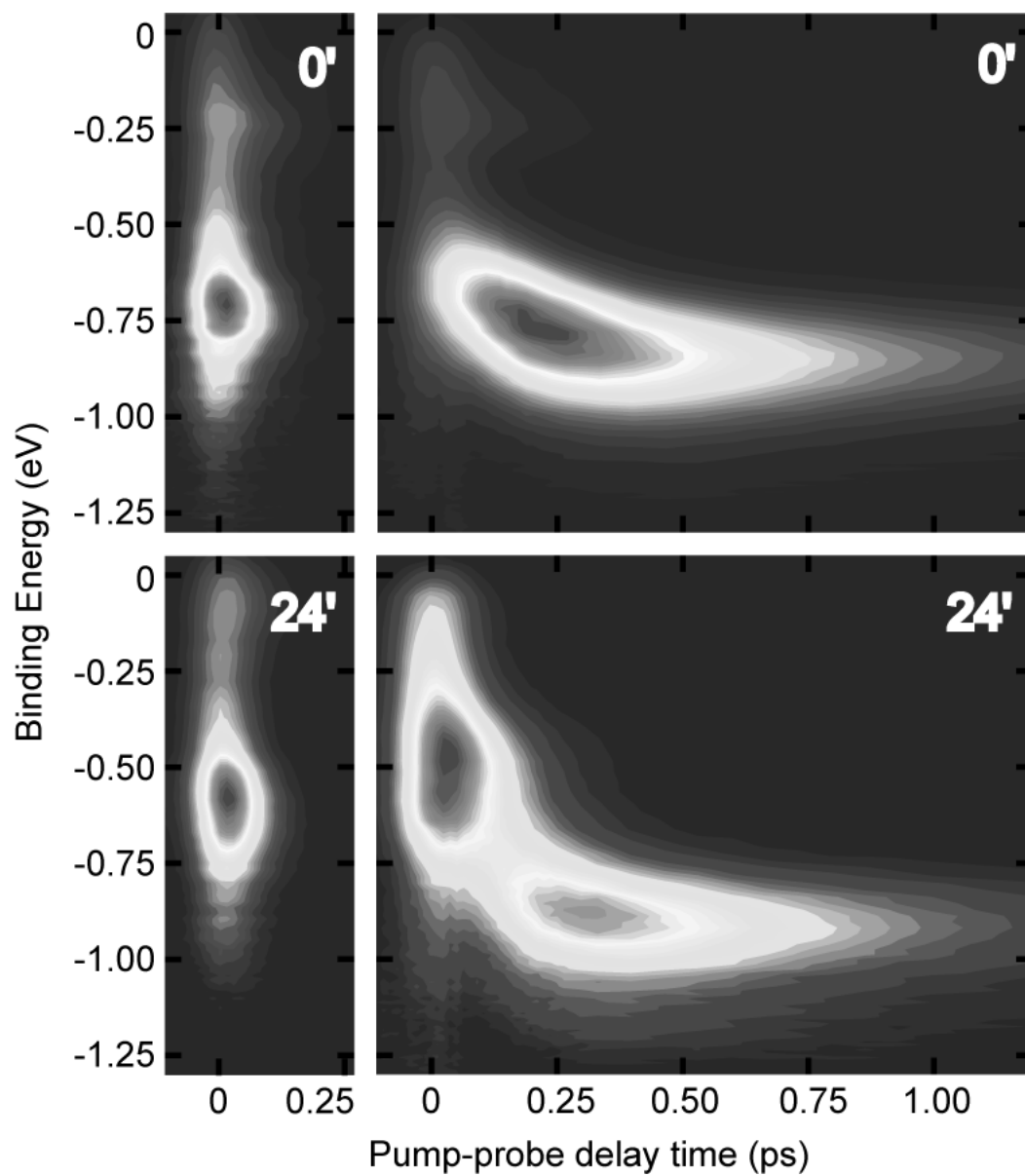


Figure 4.1: The dynamics of the $n=1$ IPS are displayed for 1 ML (left column) and 2 ML (right column) coverages of DMSO on Ag(111) at signal collection angles of 0° and 24° . Photoelectron signal intensity is indicated by shading.

4.3 Results

Kinetic energy spectra were corrected for inelastic scattering using the Shirley function,⁶² a background subtraction method originally applied to x-ray photoemission spectra and later extended to UV and visible photoemission data.^{12, 15} The Shirley function effectively removes the low-energy inelastic tail, evident in Figure 4.2 spectra, and the resulting lineshape asymmetry using only one free parameter: a proportionality constant. All figures in this chapter present spectra corrected for inelastic scattering unless otherwise noted. Peaks identified by dosing survey and dispersion data were fit to Voigt functions. The area under a Voigt is proportional to the total population of electrons photoemitted from the electronic state. The population of electrons collected at a given photoemission angle could consequently be plotted as a function of time to study population decay dynamics. Similarly, the time-dependent energetic position of a peak yielded energy relaxation dynamics. All measurements include error bars as an assessment of instrument error, not as a rigorously defined standard deviation, unless stated otherwise.

4.3.1 Coverage Identification

Dosing surveys were performed to identify monolayer and multilayer coverages, in conjunction with subsequent measurements. Experimentally, exposures were limited to a minimum of 0.35 L due to the previously observed low pumping rate

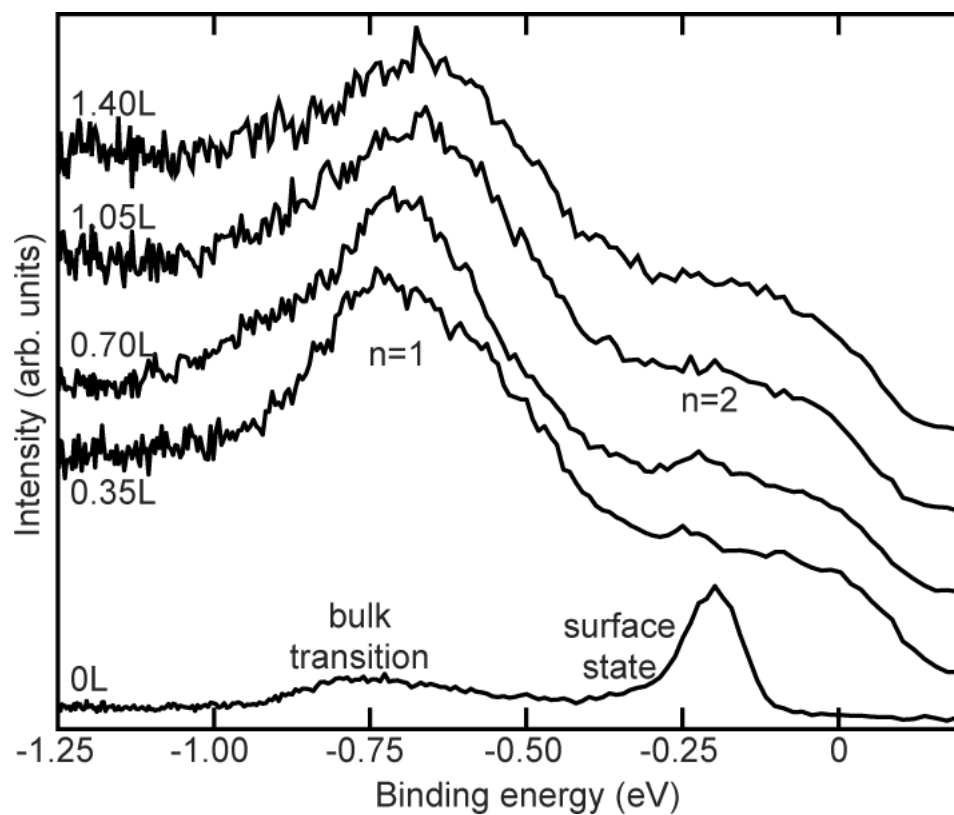


Figure 4.2: A 2PPE dosing survey of DMSO on Ag(111) is presented. The data was collected at the 1 ML voltage bias, and the spectra have not been corrected for inelastic scattering. Intensity has been scaled, and a vertical offset has been added to present the data on one graph.

of DMSO from the UHV chamber.⁵⁵ The results of a survey using minimum exposure increments are presented in Figure 4.2 with all spectra referenced to the monolayer vacuum energy and with no correction for inelastic scattering. The energy gap between the Fermi level and the clean Ag $n=1$ IPS was larger than the pump pulse energy; consequently, the only clean Ag features observed were the sp bulk transition and the low energy tail of the Shockley surface state.⁶²

As DMSO was dosed at 210 K, a new feature, the $n=1$ IPS, was observed to grow in and saturate, which is displayed in the spectrum labeled 0.7 L of exposure in Figure 4.2. Subsequent dosing at this temperature produced no further changes in 2PPE spectra or dynamics. Time-resolved scans of this coverage, however, indicated small traces of the long-lived, localized multilayer state. The coverage assigned as monolayer could only be reached after annealing the saturated coverage for 10 min at 210 K, presumably to remove small multilayer patches adsorbed at favorable nucleation sites. After annealing, no features were present from either the multilayer or the clean Ag surface. The necessity of annealing to obtain a monolayer is qualitatively in agreement with the literature.^{55, 63} Subsequent dosing at 200 K produced multilayer coverages. Multilayer thickness is reported in monolayer equivalences (ML) using a monolayer exposure of 0.5 ± 0.1 L. This value for monolayer exposure was obtained by observing saturation at 210 K in subsequent experiments with larger exposure increments. Thickness above 1 ML should be treated as a measure of average exposure, not as an assumption of layer-by-layer growth. Equation 2.1 was used to calculate a -1.20 ± 0.03 eV workfunction shift from

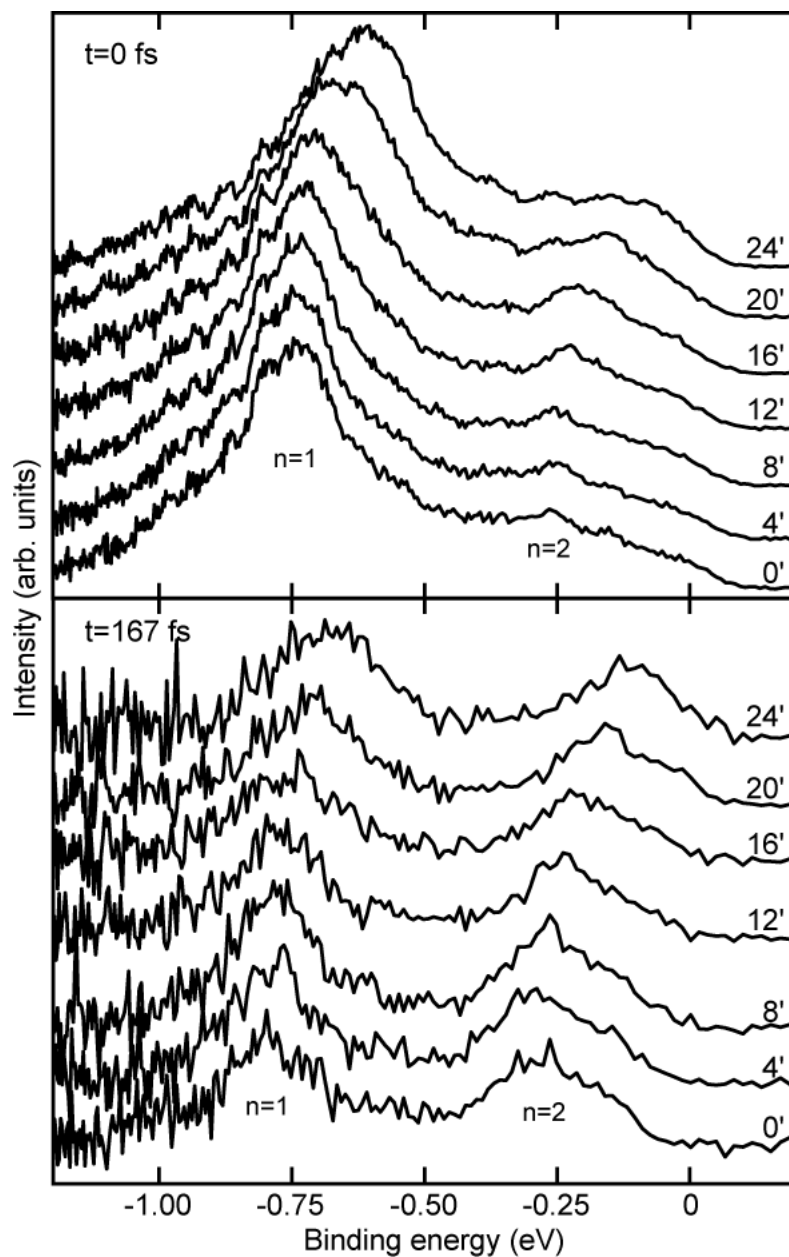


Figure 4.3: 2PPE spectra of 1 ML of DMSO are displayed at zero and long pump-probe delay times at a range of collection angles. Intensity has been scaled, and a vertical offset has been added to present the data on one graph.

1 ML of DMSO and an additional $+0.12 \pm 0.03$ eV from 2 ML of DMSO with quantum defect parameters of 0.1 and 0.15, respectively.

4.3.2 Monolayer Dynamics

A monolayer coverage of DMSO was characterized by a dispersive, short-lived, $n=1$ IPS which showed little solvation. The $n=1$ IPS peak was fit to one Voigt function at all angles, and its effective mass was determined to be $1.5 \pm 0.1 m_e$ and $1.7 \pm 0.3 m_e$ at pump-probe delays of 0 fs and 167 fs, respectively. The curvature is most evident at higher photoemission angles, where the energy shift is significantly larger than the experimental energy resolution.^{15, 64} No evidence of dynamic localization was observed, as shown in Figure 4.3. A slight dynamic increase in effective mass is seen in Figure 4.4, however the shift is small compared to error bars, and more data points would be needed to confirm this trend. Population dynamics were adequately fit to a monoexponential rise and decay⁶⁵ at all collection angles and convoluted with a Gaussian representing the instrumental response function. The data and corresponding fits for the 1 ML coverage at 0° and 24° are presented in Figure 4.5. Population decay times were found to be short at all collection angles, and the longest decay time of $\tau = 48 \pm 15$ fs was observed at 0° . Population rise times were found to be much shorter than our experimental response at all collection angles. The 1 ML solvation response was found to be small with a total energy shift of 50 ± 10 meV observed at 0° . A standard model of solvation by bulk solvents fits the response to a Gaussian and one or more exponentials.³⁰ The data bore little

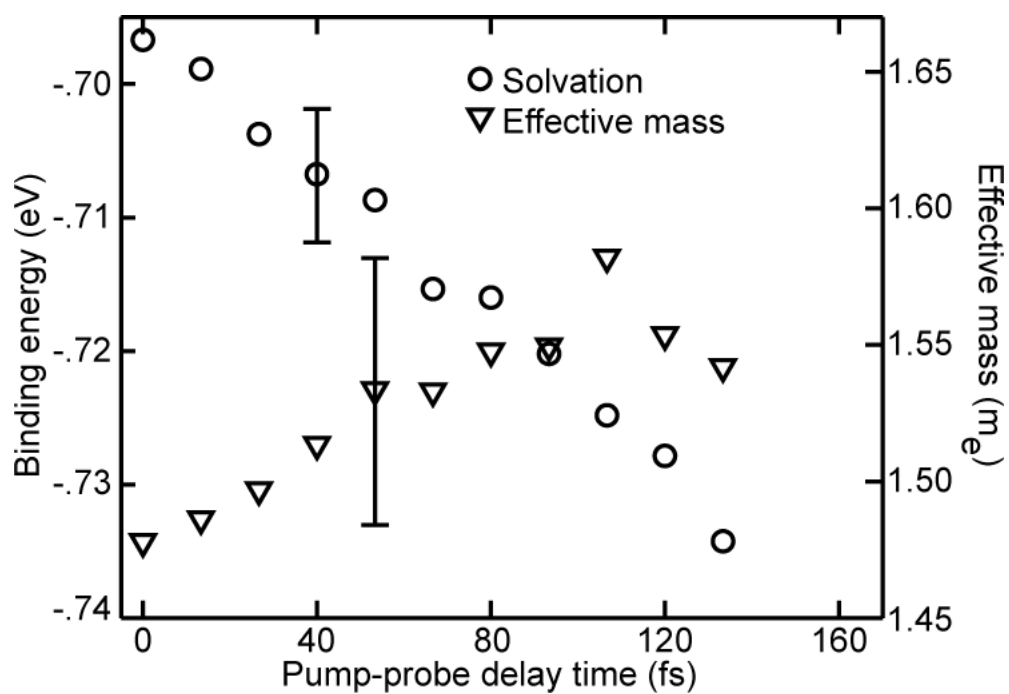


Figure 4.4: The dynamic energy relaxation at 0' and the dynamic effective mass shift are displayed for the 1 ML DMSO coverage. Decreasing signal intensity at increasing time delays contributes to greater uncertainty at longer delays.

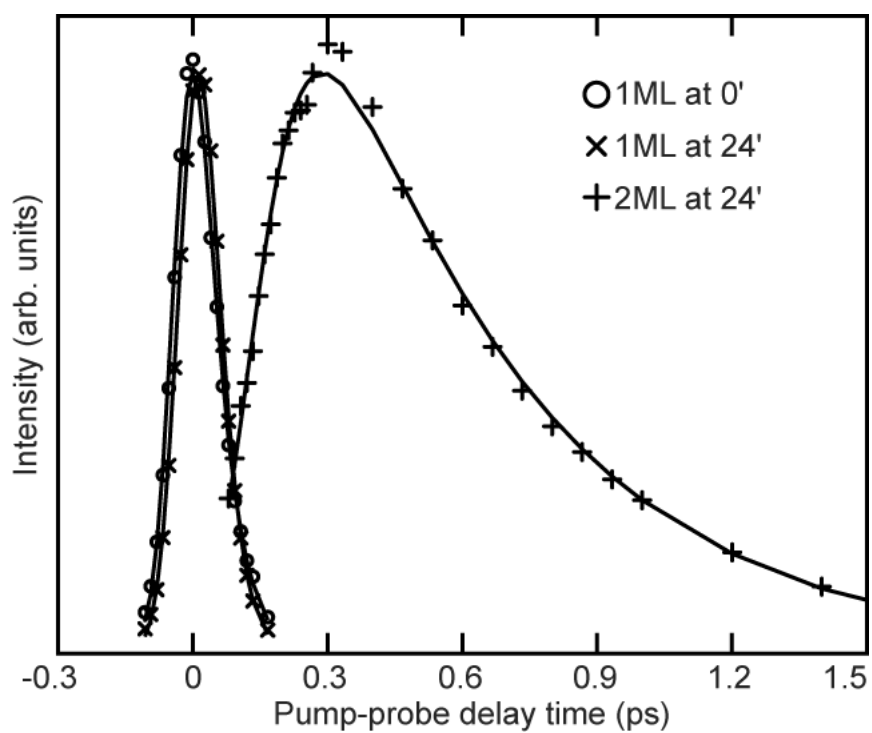


Figure 4.5: The photoelectron count intensity is plotted for the delocalized 1 ML DMSO $n=1$ IPS at 0° and 24° and the localized 2 ML $n=1$ IPS at 24° . Dots represent the actual data, and solid lines represent the fits. Intensity has been scaled to present the data on one graph.

resemblance to a Gaussian, an exponential or combination thereof, as evidenced in Figures 4.4 and 4.6. A straight line was empirically selected to fit the solvation response at all angles, and the solvation line slopes for various collection angles of the 1 ML coverage are summarized in Table 4.1 with error bars of ± 0.03 eV. Extrapolation of the solvation fit to 420 fs, the time for 95% energy relaxation of a 2 ML coverage, yields a total energy shift of 110 ± 20 meV at 0'.

Table 4.1: Linear slopes of n=1 IPS energy relaxation for 1 ML of DMSO at various collection angles

	0°	4°	8°	12°	16°	20°	24°
Slope (eV/ps)	-0.25	-0.26	-0.25	-0.26	-0.30	-0.33	-0.32

4.3.3 Multilayer Dynamics

A 2 ML coverage of DMSO was characterized by a long-lived, dynamically localizing, n=1 IPS which exhibited a large solvation response. The dynamic localization is shown in Figure 4.7, which shows an initially delocalized IPS with an effective mass of $1.2 m_e$ fully collapsing into a localized state with a slightly negative dispersion by 800 fs.

However, the extreme broadening of the state from a 340 ± 10 meV FWHM at 0' to a 440 ± 10 meV FWHM at 24' should be noted. A DMSO coverage with anisotropy in the surface-parallel plane could explain the broadening. Dipole-dipole

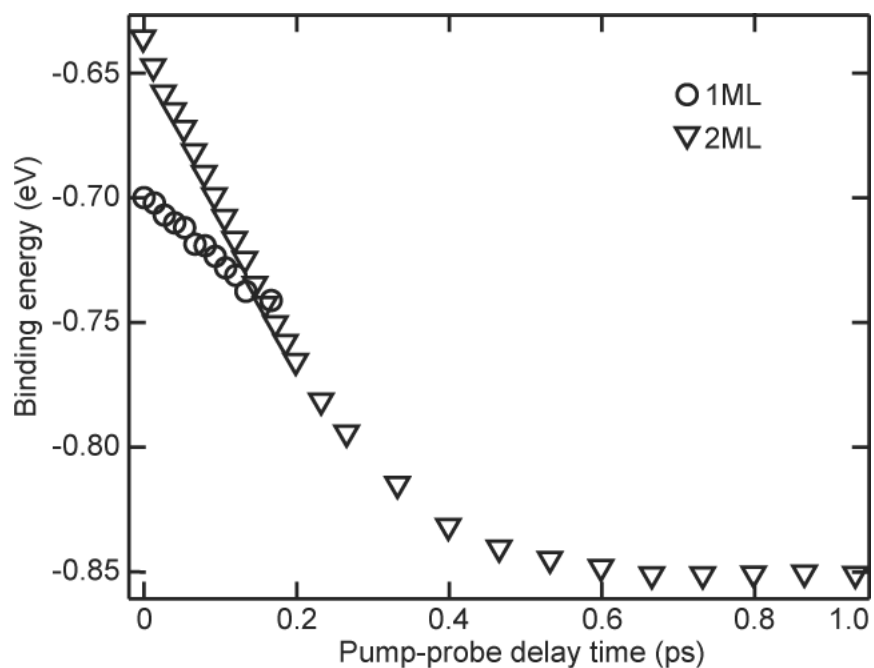


Figure 4.6: The $n=1$ IPS dynamic energy relaxation is displayed for 1 ML and 2 ML of DMSO collected at 0° . Delocalized and localized features cannot be resolved for the 2 ML coverage at 0° , and the sum of both contributions was fit to one peak. The 2 ML binding energy, therefore, primarily reflects the delocalized solvation response at early times and the localized solvation response at long times, which is dictated by the relative populations.

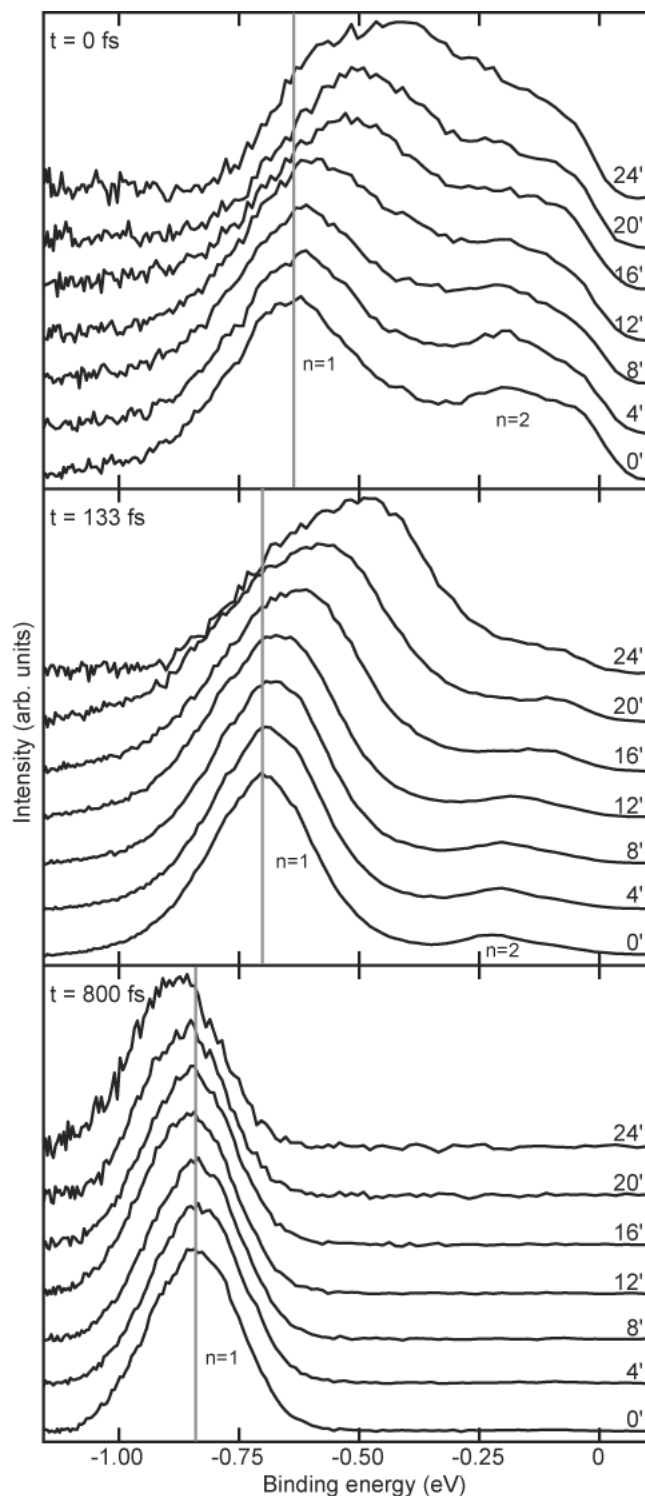


Figure 4.7: 2PPE spectra of 2 ML of DMSO are displayed at zero, intermediate and long pump-probe delay times at a range of collection angles. Intensity has been scaled, and a vertical offset has been added to present the data on one graph. A vertical line has been added at the 0° $n=1$ binding energy as a guide for the eye.

interactions induce short-range order and dipole alignment of DMSO on gold substrates.^{56, 63} The local anisotropy could readily produce a dispersion relation dependent on the electron \mathbf{k}_{\parallel} direction with respect to the dipole-induced structure.¹⁸ Collection of electrons with a specifically defined \mathbf{k}_{\parallel} direction relative to the adsorbed layer structure is prevented by the layer's lack of long-range order. The calculated effective mass of $1.2 m_e$ should only be taken as a weighted average of effective masses present in the anisotropic environment.¹⁵

The delocalized $n=1$ IPS and the localized state were well-resolved at 20° and 24° collection angles and could be cleanly fit to two peaks. Extraction of population and solvation information from the spectrally overlapped delocalized and localized states at the intermediate 12° and 16° collection angles was accomplished with the treatment of the data outlined in Section 4.5. The separation of localized and delocalized features was not possible at collection angles lower than 12° .

A monoexponential rise and decay function convoluted with a Gaussian was fit to the delocalized and localized state population dynamics. The two time constants were equal within experimental error at every collection angle for the delocalized state; consequently an assignment of one constant as a rise time and the other constant as a decay time was not possible.⁶⁵ The average of the two constants is reported in Table 4.2. While over-interpretation of data sets containing only four values should be avoided, a general trend towards longer rise and decay times at lower \mathbf{k}_{\parallel} is noted. Intra-band relaxation, described by Garrett-Roe *et al.*²⁵ and the references within, accounts for this phenomenon as electrons relax to lower \mathbf{k}_{\parallel} . However, the only inter-band decay mechanism considered by this reference is decay to the metal. The

unknown, possibly \mathbf{k}_{\parallel} -dependent rate of localization from delocalized states would severely complicate an analysis, such as the one performed by Garrett-Roe *et al.*²⁶ Consequently, the competition between inter-band and intra-band relaxation is beyond the scope of this work. A rise time of $\tau = 100 \pm 15$ fs and a decay time of $\tau = 460 \pm 40$ fs was obtained for the localized state population dynamics measured at 24° , and the data and the fit are displayed in Figure 4.5.

Table 4.2: Average of rise and decay times of n=1 IPS for 2 ML of DMSO

	12°	16°	20°	24°
τ (fs)	105	106	85	68

The 2 ML solvation response was found to be large with a total energy shift of 220 ± 10 meV observed at 0° , displayed in Figure 4.6. The 2 ML delocalized state exhibited a time-dependent energy relaxation best fit to a straight line at collection angles of 12° and larger. For the data collected at 12° , 16° , 20° and 24° , the localized state energy shift was adequately fit to a single exponential, but the standard model of a Gaussian and an exponential component was also tested and found unnecessary. As discussed in Section 4.5, the localized state exponential relaxation times and Gaussian widths are expected to be invariant to photoemission angle. The exponential relaxation time averaged across collection angles was 140 fs with a 15 fs standard deviation using a single exponential relaxation. Using the Gaussian plus exponential model, an average exponential relaxation time of 165 fs with a 20 fs standard

deviation and average Gaussian FWHM of 210 fs with a 70 fs standard deviation was observed. The large standard deviation of the Gaussian FWHM indicates that it might not be a useful or necessary component to describe the 2 ML solvation.

4.4 Discussion

A number of results are singular or otherwise merit further discussion: 1) our coverage assignment was benefited by literature DMSO thin film growth studies, 2) the population decay time increase from 1 ML to 2 ML of DMSO is quite large, and 3) the solvation response of the 2 ML coverage is much larger than for the 1 ML coverage.

4.4.1 Coverage Assignment: Comparisons to the Literature

Coverage assignment was verified by thermal desorption spectroscopy (TDS) and Kelvin probe measurements of DMSO ultrathin films on Au(111) and Au(100).⁵⁵ Both techniques indicated maximum monolayer desorption rates at temperatures ~30 K higher than maximum multilayer desorption. DMSO 2PPE features and the majority of the workfunction shift were observed in our experiment after monolayer exposure times at 220 K. However, complete extinction of clean Ag(111) surface features was never observed at 220 K despite exposures as large as 3 ML equivalence. Neither TDS or Kelvin probe results would be expected to distinguish a saturated monolayer from a monolayer with small, exposed metal patches, which is a confirmed

morphology on Au(111) and Au(100) by STM.⁶³ Consequently, we believe the 20 K difference between the nearly-saturated monolayer and the multilayer dosing temperatures on silver agrees well with the difference in maximum desorption temperatures on gold.

The Kelvin probe measurements of DMSO on Au(100) reported a workfunction shift of -.62 eV associated with the monolayer, followed by a smaller additional -.15 eV shift attributed to the multilayer.⁵⁵ The 1 ML and 2 ML workfunction shifts were calculated from Equation 2.1 to be $-1.20 \pm .03$ eV and $-1.08 \pm .03$ eV, respectively, with quantum defect parameters of .1 and .15. Similar to the results on gold, monolayer dosing resulted in the majority of the workfunction shift, and multilayer dosing produced only small changes. Partial charges on metal and sulfur atoms are expected to be larger at the silver interface than at the gold interface, and this property is noted to explain the larger magnitude workfunction shift of 1 ML of DMSO on silver.⁶⁶ Efficient charge transfer, resulting from the stronger silver-sulfur interaction, followed by reduced charge transfer to subsequent layers is proposed to explain the +.12 eV shift between 1 ML and 2 ML, as reported for other systems with strong substrate/adsorbate interactions.²⁰

4.4.2 Population Decay Times

The 2 ML IPS clearly decayed back to the metal on a much longer timescale than the 1 ML IPS. This behavior was consistent with a number of systems in which electrons were pushed to the outside of the adsorbed layer, and the additional

tunneling barrier hindered efficient decay to the metal.^{25, 67} However, the localization present in 2 ML could solely explain the decay time increase, and a 3 ML coverage was examined to verify this mechanism. A monoexponential rise and decay were inadequate to fit population decay, and a biexponential decay produced a much better fit than a stretched exponential. Decay times of $\tau = 440 \pm 40$ fs and $\tau = 5.6 \pm 0.5$ ps were calculated for the 3 ML localized state at 24°. An order of magnitude decay time increase is expected when pushing the electron 1 ML further from the metal surface. The extra stabilization provided by an additional DMSO layer to a localized state residing in the adsorbed layer should be weak and is insufficient to explain the large decay time increase between 2 ML and 3 ML.^{2, 41} The 3 ML decay time confirms that the IPS resides outside the adsorbed DMSO coverage. Additionally, the 2 ML delocalized state decay times are significantly greater than the 1 ML decay times, despite the additional decay channel via localization, which further supports the conclusion that IPS electrons are pushed to the outside of the adsorbed layer.

4.4.3 Dynamic Energy Relaxation Mechanisms

An analysis of interfacial electron population and energy relaxation dynamics at D₂O/Ru(001) and D₂O/Cu(111) interfaces has conclusively shown energy relaxation that does not result from solvation,²³ and this mechanism must be considered in the context of the current results (Section 2.4.1). Solvation-independent energy relaxation can occur when decay times of interfacial electrons are faster for higher energy states. A dynamic shift of peak maximum to lower energies is observed as higher energy

contributions to an inhomogeneously broadened peak decay more quickly than lower energy contributions. All population decay dynamics of an inhomogeneously broadened peak resulting from this mechanism will lie within the peak envelope of the feature at its maximum population. A dynamic shift of the feature outside of the peak envelope reflects a real energy shift of the inhomogeneous distribution, and another mechanism, i.e. solvation, must be included. Using this criterion, the energy relaxation observed in 1 ML of DMSO could be wholly attributed to energy-dependent decay times. The 2 ML data stands in contrast: both the localized state observed at 24° and the combination of solvated features observed at 0° dynamically shift significantly outside their peak envelopes. In summary, the 2 ML coverage exhibits solvation, while the 1 ML coverage might not solvate. The following section attributes all energy relaxation to solvation; a complete lack of monolayer solvation would underscore these results.

4.4.4 The Image Potential State as a Capacitance

Molecular dipole reorientation has previously been shown to cause dynamic energy relaxation of IPS's in UHV experiments.^{13, 39} A rotationally frustrated monolayer molecular dipole has been previously proposed to explain the low interfacial capacitance of DMSO measured by electrochemistry. The unifying physical process connecting bulk DMSO electrochemical capacitance to the dynamic energy relaxation measured in this experiment is molecular dipole reorientation. Electrochemical measurements obtain bulk values for the entire solvent, and the

variation of experimental parameters can be used to draw conclusions about monolayer (Helmholtz layer) and multilayer (Gouy-Chapman layer) contributions. A 2PPE experiment is able to separately study monolayer and multilayer coverages and directly observes layer-dependent dielectric response to injected charge. Across the shared time range when both 1 ML and 2 ML features were observable, the 2 ML response was significantly greater. The 2 ML response was also significantly greater than the 1 ML response extrapolated to 420 fs, the time required for 95% energy relaxation in a 2 ML coverage. The smaller solvation response of the monolayer compared to the 2 ML multilayer is due to the decreased rotational reorientation of the monolayer coverage. The frustrated monolayer reorientation inferred from bulk measurements is evident in this experiment, which draws an explicit connection between in situ measurements and our model electrode interface.

In an attempt to draw an analogy between electrochemical interfacial capacitance and the energy shifts due to solvation, a simple model for the dynamic energy shift is suggested. One should not take this model in any quantitative sense, but rather we develop it more for its pedagogical value. The IPS consists of a charge separation between the electron and its image. This charge separation is held at a potential corresponding to the spacing between the Fermi level and $n=1$ IPS. Viewed in this context, the IPS and its image could be considered as a capacitance. We will recast the solvation dynamics in the context of capacitance and the dielectric constant.

As an example of the capacitive nature of the system, a simple prediction of the size distribution of IPS electrons at the Ag(111)/vacuum interface is made. Equation 4.2 states capacitance (C) in terms of charge (Q) and potential (V) and in

terms of the vacuum permittivity (ϵ_0), the dielectric constant (ϵ), plate area (A) and plate spacing (d) for a parallel-plate capacitor configuration.

$$C = \frac{Q}{V} = \epsilon_0 \epsilon \frac{A}{d} \quad (4.2)$$

A gross assumption of homogeneous electron and image charge distributions across a given surface area (A) at the surface normal direction IPS expectation value (d) reduces the IPS and its image to the parallel-plate situation. The situation is illustrated in Figure 4.8. Inserting known, measurable quantities for charge, potential, vacuum permittivity, a dielectric constant of one and the expectation value for $n=1$ in the surface normal direction, Equation 4.2 predicts a plate diameter of 14 Å.

The dielectric constant used in Equation 4.2 can be separated into three components of dielectric response for generic media, as specified in Equation 4.3.

$$\epsilon = \epsilon_{ion} + \epsilon_{mol} + \epsilon_{el} \quad (4.3)$$

The ionic component (ϵ_{ion}) is non-existent in the current experiment. The electronic component (ϵ_{el}) occurs on a timescale faster than our 2PPE measurements can detect⁶⁸ and does not contribute to the dynamic response. Only the molecular component (ϵ_{mol}), consisting of dipole rotation and molecular vibrations, contributes to the dynamic dielectric response measured by the current experiment.

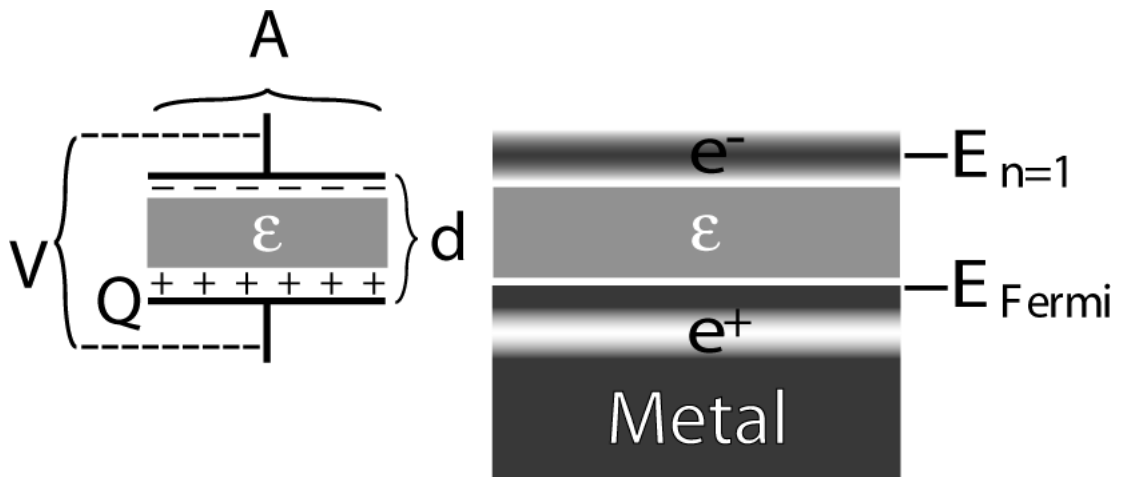


Figure 4.8: The similarity between the configuration of an electron and its image in the image potential state and a parallel-plate capacitor is illustrated.

Energy relaxation times due to ϵ_{mol} are highly solvent dependent in bulk solution and can be in excess of nanoseconds. However, DMSO exhibits relatively rapid solvation as observed by Horng *et al.* from the time-resolved Stokes shift of coumarin 153 in DMSO solution,³⁰ which is consistent with other solvents that lack a hydrogen bond network. They find that the majority of the energy relaxation is described with a 0.214 ps exponential decay time, and the longest decay time of 10.7 ps comprises less than 10% of the total energy relaxation. The localized state is visible at pump-probe delays as large as 2.2 ps in the 2 ML coverage; therefore, the current experiment has access to the time range in which 75% of the ϵ_{mol} dielectric response occurs in bulk.³⁰ However, the current experiment is conducted in the presence of an interface at temperatures much reduced compared to the bulk solvent, which could potentially introduce new librational modes and slow large-scale collective solvent motions.

A capacitance can be calculated at a pump-probe delay of 0 fs from the $n=1$ IPS energy above the Fermi level. This effectively measures the capacitance before the ϵ_{mol} component can contribute to energy relaxation. A long-time capacitance measurement probes capacitance after complete relaxation from the ϵ_{mol} contribution. This circumstance is equivalent to measuring the capacitance between two plates with and without a dielectric medium of ϵ_{mol} between them. The situation is described by Equations 4.4:

$$C_i = \epsilon_{el} C_{vac} \quad (4.4a)$$

$$C_f = \epsilon_{el} C_{vac} + \epsilon_{mol} C_{vac} \quad (4.4b)$$

where the 0 fs capacitance (C_i) and long-time capacitance (C_f) are defined relative to C_{vac} , the capacitance without a dielectric. The electronic and molecular components of

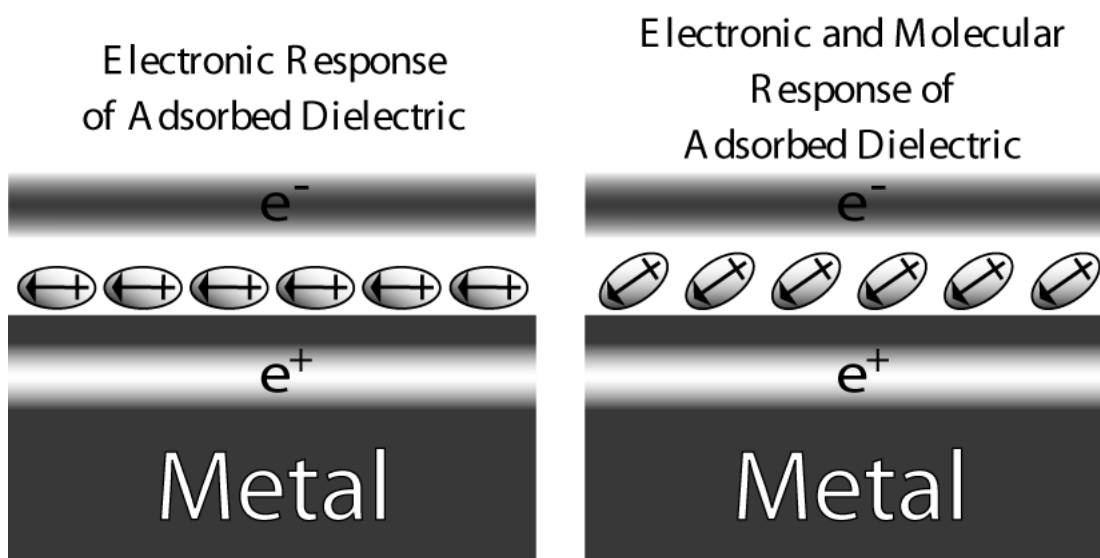


Figure 4.9: The electron density in the metal, adsorbed layer and image potential state are represented by shading. Molecular dipoles, prior to perturbation by the electron and its image, are represented by arrows. The left panel depicts C_i . The shading of the adsorbed molecules indicates that the electron density has already equilibrated to the electric field established between the electron and its image. The right panel depicts C_f . In addition to the electronic response, the molecular coordinate has equilibrated to the IPS electric field.

relaxation are also illustrated in Figure 4.9. Simple substitution eliminates the unmeasured C_{vac} term and expresses ϵ_{mol} as a fraction of ϵ_{el} in Equation 4.5.

$$\frac{C_f}{C_i} = 1 + \frac{\epsilon_{mol}}{\epsilon_{el}} \quad (4.5)$$

In the context of the DMSO results, instantaneous and long-time capacitance measurements can be used to determine the ϵ_{mol} contribution in terms of ϵ_{el} for various DMSO coverages. A reasonable value for ϵ_{el} of 2.19 can be obtained for DMSO by equating ϵ_{el} to the dielectric response high frequency limit (ϵ_{∞}), which is derived using $\epsilon_{\infty} \approx n_D^2$ from the index of refraction (n_D).³⁰ Insertion of the ϵ_{el} value allows for ϵ_{mol} determination from the observed, fractional $\epsilon_{mol}/\epsilon_{el}$.

Table 4.3: Electrochemical Model Predictions for 1 ML and 2 ML of DMSO

	1 ML	2 ML
Cap at t=0 (F)	6.0×10^{-20}	5.6×10^{-20}
Cap/A at t=0 (F/ cm ²)	7.7×10^{-8}	7.2×10^{-8}
Cap at t→∞ (F)	$6.1-6.3 \times 10^{-20}$	6.1×10^{-20}
Cap/A at t→∞ (F/cm ²)	$7.8-8.0 \times 10^{-8}$	9.3×10^{-7}
ϵ_{mol}	.034-.091	.18
$\epsilon_{mol}(\text{Area corr.})$.034-.091	26

Cap = capacitance; Cap/A = capacitances per unit area;
 ϵ_{mol} = dielectric constant; $\epsilon_{mol}(\text{Area corr.})$ = area corrected dielectric constants

Capacitance and ϵ_{mol} were calculated for the 1 ML and 2 ML coverages and summarized in Table 4.3. It is curious to note the similarity of long-time capacitances between both coverages, however the combination of effects by which this

circumstance occurs implies coincidence. Initial capacitances (C_i), and presumably C_{vac} , are distinct between coverages, which result from the differing static workfunctions of the 1 ML and 2 ML coverages. The higher initial energy of the $n=1$ IPS in the 2 ML coverage, due to the larger workfunction, is countered by the larger ϵ_{mol} of the 2 ML coverage. Consequently, the final energy above the Fermi level of the solvated electron in the 2 ML coverage is equal to the energy of the solvated electron in the 1 ML coverage from the combination of static workfunction and dynamic ϵ_{mol} contributions.

A variety of treatments were employed to report the data more accurately. The 1 ML coverage showed no long-time asymptote. A range of long-time capacitances for the 1 ML coverage was established by defining two limiting cases. The lower limit was defined by the capacitance at the longest measurable pump-probe delay; long-time IPS energy could not be higher than this value. The upper limit was obtained by considering the solvation timescale of the 2 ML coverage. The molecular response of the monolayer directly adsorbed to the substrate contributes to the observed energy relaxation of the 2 ML coverage. Consequently, the long-time asymptote in the 2 ML energy relaxation dynamics demonstrates the complete relaxation of the directly adsorbed monolayer. While the increased distance and dielectric screening between an electron and the directly adsorbed monolayer in a 2 ML coverage might affect the monolayer relaxation magnitude and could lengthen the relaxation timescale of the adsorbed monolayer with respect to the 1 ML coverage, the asymptotic energy relaxation defines an upper limit for the monolayer solvation timescale. The extrapolation of the monolayer linear solvation response to the 3τ

relaxation time of the 2 ML coverage (420 fs) provides a potential from which a capacitance upper limit is calculated. The true long-time capacitance resides within these limits.

Capacitances for the 2 ML coverage were calculated using dynamics collected at 0° . At this collection angle, the delocalized $n=1$ IPS and the localized state could not be resolved, and one Voigt function fit the combination of these features. Ideally, the delocalized $n=1$ IPS energy relaxation dynamics collected at 0° would be used. This collection angle was chosen to eliminate potential contributions of dynamic effective mass shifts to observed energy shifts. If this consideration were ignored, the localized state collected at 24° exhibits an energy shift of 190 ± 10 meV from its initial detection at a 90 fs delay time.

Capacitances per area were reported to highlight the magnitude of the capacitance, otherwise obscured by the small model plate area. Estimates of plate area were made from earlier determinations of the coherence lengths of interfacial delocalized electrons (~ 100 Å)¹³ and the $\pm 2\sigma$ width of a 17 Å FWHM Gaussian-shaped localized state.²⁰ This correction especially affects the 2 ML ϵ_{mol} computation due to dynamic shrinkage of the model plate via electron localization. Necessarily, the corrected and uncorrected 2 ML ϵ_{mol} are interpreted as upper and lower limits of the true value.

The results of ϵ_{mol} calculations recast the conclusion already reached: the 2 ML coverage has a much larger solvation response to excess charge. Uncorrected for plate area considerations, 2 ML of DMSO has an ϵ_{mol} of 2.0 - 5.2 times that of 1 ML of DMSO. A correction for dynamic plate shrinkage in 2 ML of DMSO increases its ϵ_{mol}

relative to 1 ML of DMSO. Whether area corrected or not, unique responses are obtained for the monolayer and multilayer, confirming experiments in bulk solvent.

4.5 Advanced Fitting Procedures

It is clear from Figure 4.7 that the localized state and delocalized IPS's overlap significantly at collection angles lower than 20° for a 2 ML coverage of DMSO. A rigorous fitting procedure is required to capture the population and energy relaxation dynamics of this system.

4.5.1 Apparent Negative Effective Mass

First, however, the negative dispersion of the localized feature must be considered. A distribution of localized electronic states with localization sizes dependent on binding energy can cause a negative dispersion to be observed.⁶⁹ Population decay dynamics are used to distinguish between a collection of localized states with a negative dispersion and a delocalized state with a truly negative effective mass. While angle-resolved dynamics of a delocalized electronic state selectively sample sub-sets of the population with well-defined \mathbf{k}_{\parallel} values, angle-resolved dynamics of a localized state sample the same population at a distribution of angles. Delocalized electrons possess intra-band scattering mechanisms between \mathbf{k}_{\parallel} states, resulting in varying decay times across \mathbf{k}_{\parallel} states. A collection of localized states does

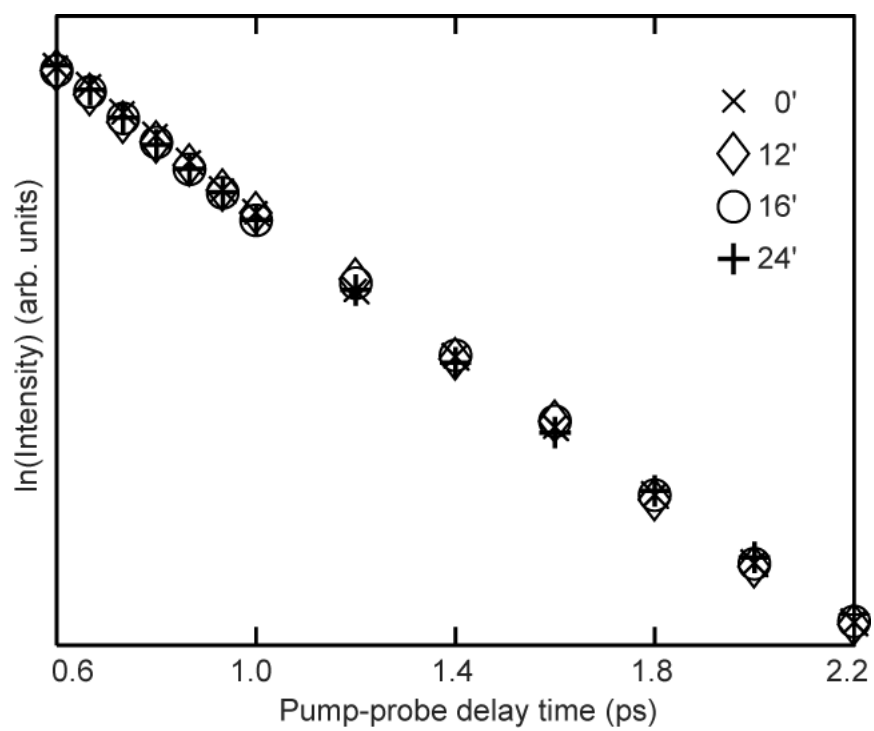


Figure 4.10: The long-time localized state population decay is plotted in natural log scale as a function of time at a range of collection angles for the 2 ML DMSO coverage. Intensity has been scaled to present the data on one graph.

not possess intra-band scattering mechanisms, and the decay times are invariant to photoemission angle.

At long pump-probe delay times (> 600 fs), the delocalized IPS was not observed for the 2 ML coverage, and the localized state decay time was obtained by a fit to a single exponential. Figure 4.10 shows the long-time population decay of the localized IPS feature at multiple angles. The invariance of decay time to collection angle is a strong indication that the negatively dispersive feature is a collection of localized states.

4.5.2 Extraction of Delocalized State Dynamics

The long-time invariance of the localized state decay constant was used to fit spectra collected at 12° and 16° . While the decay time was invariant to angle, the signal intensity was not. The monoexponential rise and decay function that fit the 24° population dynamics was multiplied by an intensity scaling parameter. The value of the parameter was calculated by least-squares minimization of the long-time intermediate angle intensities to the scaled 24° population dynamics fit. The data in Figure 4.10 are displayed with similar intensities by using these scaling factors. At short and intermediate pump-probe delay times, the localized state intensity was constrained to values within two standard deviations of the scaled 24° intensity. Similarly, the peak position of the localized state was constrained to reside between the 24° localized state peak position and the 0° peak position of the combined localized and delocalized state. Delocalized state dynamics could be successfully

extracted using these localized state constraints for 12° and 16° data, which results in fits of delocalized and localized state dynamics at a total of four collection angles: 12°, 16°, 20° and 24°. At lower collection angles, the delocalized and localized features overlapped too closely, and successive fitting attempts resulted in a largely varying delocalized state intensity.

4.6 Conclusion

The calculated capacitances and dielectric constants discussed above can only be viewed qualitatively because of the inherent assumptions and corrective factors. The simplest interpretation comes directly from the measured solvation data, which clearly indicate a larger, fundamentally different molecular response for 2 ML of DMSO compared to 1 ML of DMSO. A direct observation has been made in vacuum to confirm a phenomenon postulated from bulk electrochemical measurements, and a connection between the fields of UHV and electrochemical surface science was reinforced.

Chapter 5: Implementation of Thermal Desorption

Spectroscopy in the Current UHV Chamber

5.1 Thermal Desorption Spectroscopy

Thermal desorption spectroscopy (TDS) is a simple technique that provides clear information on the growth morphology, desorption kinetics and thickness of adsorbed thin films. Thermal desorption spectroscopy relies on the temperature-dependent desorption rate of an adsorbate from a surface. The desorption rate is expressed in Equation 5.1:

$$-\frac{d[A]}{dt} = k_0 \times [A]^n \times e^{-\frac{E_A}{kT}} \quad (5.1)$$

which is commonly referred to as the “Redhead model”, referencing the seminal work of Redhead.⁷⁰ In Equation 5.1, the desorption rate ($-d[A]/dt$) of species A depends on its concentration on the surface ($[A]$) to the order of the reaction (n). Molecules of species A can be thought to attempt a desorption event with some frequency k_0 corresponding to a vibration with components normal to the surface. The act of desorption requires some amount of energy E_A , and the fraction of molecules possessing sufficient energy to desorb is given by a temperature-dependent Boltzmann factor.

Redhead discusses a linear ramp of temperature as a function of time for use in desorption experiments, which is commonly referred to as the “Redhead method” or

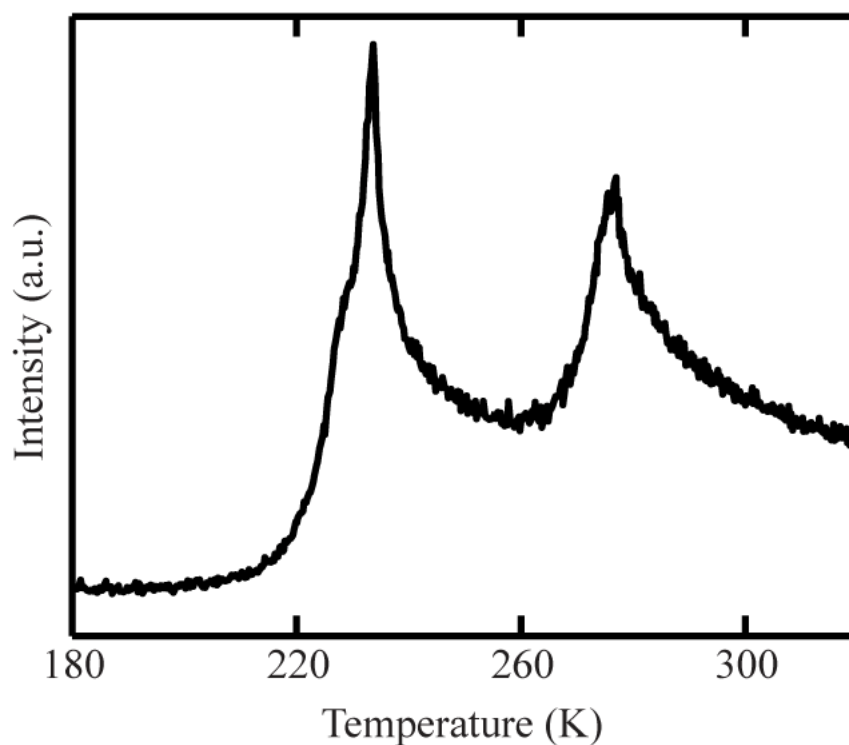


Figure 5.1: A TPD spectrum measured at a mass/charge ratio of 56 amu/e of a thin film of butanol between 2 – 3 ML in thickness adsorbed on an Ag(111) substrate. The peak at 275 K is saturable and corresponds to desorption of the first monolayer. The peak at 233 K corresponds to desorption of additional monolayers. Signal at the peak itself comes primarily from the second monolayer, and the low-temperature bulge arises from small contributions to desorption from the third and/or higher monolayers.

temperature-programmed desorption (TPD). Desorbed material is commonly detected with a mass spectrometer. The signal from detected material is plotted as a function of substrate temperature and is proportional to the desorption rate in Equation 5.1. A representative TPD spectrum collected with our experimental apparatus is shown in Figure 5.1. The peak shape of a desorption feature in a TPD spectrum is exponential at low temperatures (i.e. early times) as a result of the Boltzmann factor in Equation 5.1. At higher temperatures, the depletion of the adsorbed layer becomes significant, and the observed signal is reduced. A desorption energy can be extracted by fitting an exponential to the low temperature portion of the spectrum where depletion effects are negligible.

A number of properties of ultrathin films can be extracted from TPD studies. The number of desorption features in a TPD spectrum can indicate the number of energetically distinct adsorption environments present at the interface. TPD can distinguish adsorption energy differences arising from adsorption on the bare substrate versus adsorption on other adsorbed molecules or adsorption at atomically flat terraces versus adsorption at defects and step edges.^{55, 71, 72} Additionally, dosing procedures for film growth can be determined using TPD. The integrated area of a desorption feature corresponds to the total amount of material desorbed. A study of dosing time versus integrated peak area can indicate the saturability of a feature and the corresponding thin film coverage.^{73, 74} Appropriate dosing and annealing temperatures can be selected by observing the temperatures at which films desorb. Furthermore, these data can be extracted for multicomponent thin films with the molecular specificity of mass spectrometric detection, and the relative concentration of

components in a multicomponent thin film can be determined from integrated peak areas and mass spectrometer response factors.

5.2 Component Synchronization for TPD Measurements

Multiple requirements have already been specified that are necessary to conduct a TPD experiment. Substrate temperature control must be capable of producing a linear ramp rate. Typical ramp rates in TPD experiments range between 1 – 5 K/s. The mass spectrometer must be capable of rapid, precise data logging to accurately record the shape of a desorption peak. A monolayer coverage can fully desorb in less than 5 s, and it is highly desirable to describe the desorption peak with twenty or more data points; therefore, a mass spectrometer sampling rate of 4 Hz or higher is also required.

Finally, the logging of temperature and mass spectrometer data must be synchronized to provide a TPD spectrum. Synchronization is feasibly accomplished by PC-controlled data acquisition and time stamping of data. The mass spectrometer was purchased with software included that quickly logs and time stamps data. However, I wrote the software for temperature control from the PC. Simultaneous execution of both the mass spectrometer and temperature control software from the same PC has allowed TPD to be performed on a number of thin films. The system was calibrated with xenon and naphthalene thin films, which have well-characterized TPD spectra in the literature.^{75, 76} Since its implementation, TPD has provided a useful surface characterization technique for thin films of DMSO, butanol/water

mixtures, toluene, various lengths of thiophenes, room-temperature ionic liquids and other materials.

5.3 Theory of PID Temperature Control

The hardware for substrate temperature control was described previously in Section 3.4. Briefly, sample temperature input from a thermocouple is used to determine the correct, signal output to a variable power supply (up to ~45 W), which powers a resistive heater located under the sample. A brief lag exists between the application of power to the heater and a detectable thermocouple response. The lag presumably results from the time required to transmit heat through the sample. The method, by which the *correct* power output is determined to provide stable substrate temperatures in the presence of a lagged response, is proportional, integral, derivative (PID) temperature control. PID control theory is well-developed⁷⁷ and can provide, rapid, precise control of a target variable, in our case the control of temperature. For our purposes, the temperature controller must provide 1) a rapid transition to a specified target temperature for dosing, sputtering and annealing with a low overshoot and sub-Kelvin stability and 2) a stable, linear temperature ramp.

The silver substrate can be thought of as a system in thermal contact with a surrounding bath. Following a thermal perturbation, the sample will return to the bath temperature as heat flows from the sample to the bath. The rate of heat transfer (dQ/dt) is linearly proportional to the difference in temperature between the sample and bath (ΔT), expressed in Equation 5.2.⁷⁸

$$-\frac{dQ}{dt} = k\Delta T \quad (5.2)$$

Consequently, the relaxation of sample temperature plotted as a function of time has an exponential shape. Empirically, the linear heat flow model of Equation 5.2 reproduces the observed thermal relaxation of the substrate rather well and will be used for temperature control simulations below. The bath temperature in our experimental apparatus is either room temperature or a cryogenically cooled base temperature of ~ 130 K using liquid nitrogen cooling.

5.3.1. Proportional Response

Proportional control produces an output (P) proportional to the difference between the sample temperature (T) and a preset, target temperature (T_0), and the proportionality is determined by a constant (k_P). Equation 5.3 specifies the behavior of a proportional control device.

$$P = -k_P \times (T - T_0) \quad (5.3)$$

The proportionality constant k_P is an system-specific, empirically derived parameter in the control algorithm. For the current experimental apparatus, a positive value of k_P can only be obtained by defining the right-hand side of Equation 5.3 with a negative sign. When the sample temperature is less than the target temperature, heating is needed. Consequently, when $T - T_0$ is negative, a positive value of P to the power supply is required, which necessitates the insertion of a negative to preserve a positive k_P . The sign of k_P is chosen to be positive by convention.

While some control algorithms require nothing more than proportional control, the drawback of such a setup is apparent near the target temperature. When $T = T_0$, the proportional output from Equation 5.3 is unavoidably zero. As a result, no heating occurs when the substrate is at the target temperature, and the onset of cooling will quickly remove the substrate from the target temperature. Thus, a proportional control is inherently unstable at the target temperature.

Two cases of instability are illustrated in Figure 5.2. These cases are generated from numerical simulations using Equation 5.2 for cooling and Equation 5.3 to provide proportional heating. A lag time is inserted between the proportional output and its effect on substrate temperature which emulates the lag time present in the experimental apparatus. Additionally, a maximum heating rate is imposed, which reflects the power limit of the resistive heater. The proportionality constant k_p may be set too low, as in the upper panel. In this case, the target temperature is never reached. In the lower panel, k_p is set too high. The temperature oscillates around the target temperature, and an initial temperature spike greatly exceeding the target temperature is present.

The needed precision for a given application determines whether the aberrations present in Figure 5.2 are acceptably small. The simplicity of a proportional-only controller is advantageous for many applications. However, an implementation of the low k_p case in our apparatus produces sample temperatures 5 K or lower than the target temperature, with the magnitude of $T - T_0$ proportionally dependent on the difference between substrate and base temperature. Both the temperature-dependent error in sample temperature and the slowness of the response

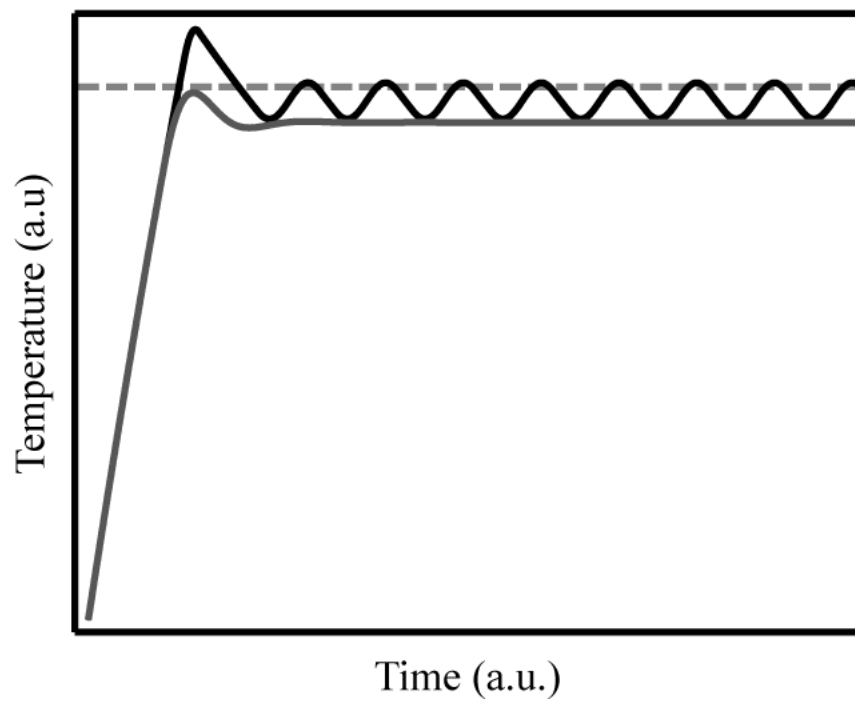


Figure 5.2: Numerical simulations of proportional controllers using low- k_p (grey) and high- k_p (black) values are displayed. The target temperature is indicated by the dotted line.

of a low- k_P proportional controller prohibit its use in our apparatus. A high- k_P proportional controller produces periodic oscillations with peak-to-trough amplitudes of 10 K or larger and is consequently unsuitable for our purposes. A more complex control system is required.

5.3.2 Integral Response

Integral control produces an output (I) proportional to the difference between the sample temperature and the preset, target temperature integrated over time. The proportionality is determined by a constant (k_I). Equation 5.4 specifies the behavior of an integral control device.

$$I = -k_I \times \int_0^t T(t) - T_0 dt \quad (5.4)$$

Alone, an integral controller functions similarly to a much lagged proportional controller. The difference between integral control and proportional control is that an integral control can have non-zero output at T_0 and will eventually reach the target temperature in a low- k_I setup. However, because of its slow response, integral control is generally used in conjunction with proportional control, referred to as a PI controller. The output of a PI controller is the sum of P and I components. Typical implementations of PI control rely on the proportional component for the majority of the output when the substrate temperature is far from the target temperature, while the integral component corrects for proportional undershooting near the target temperature.

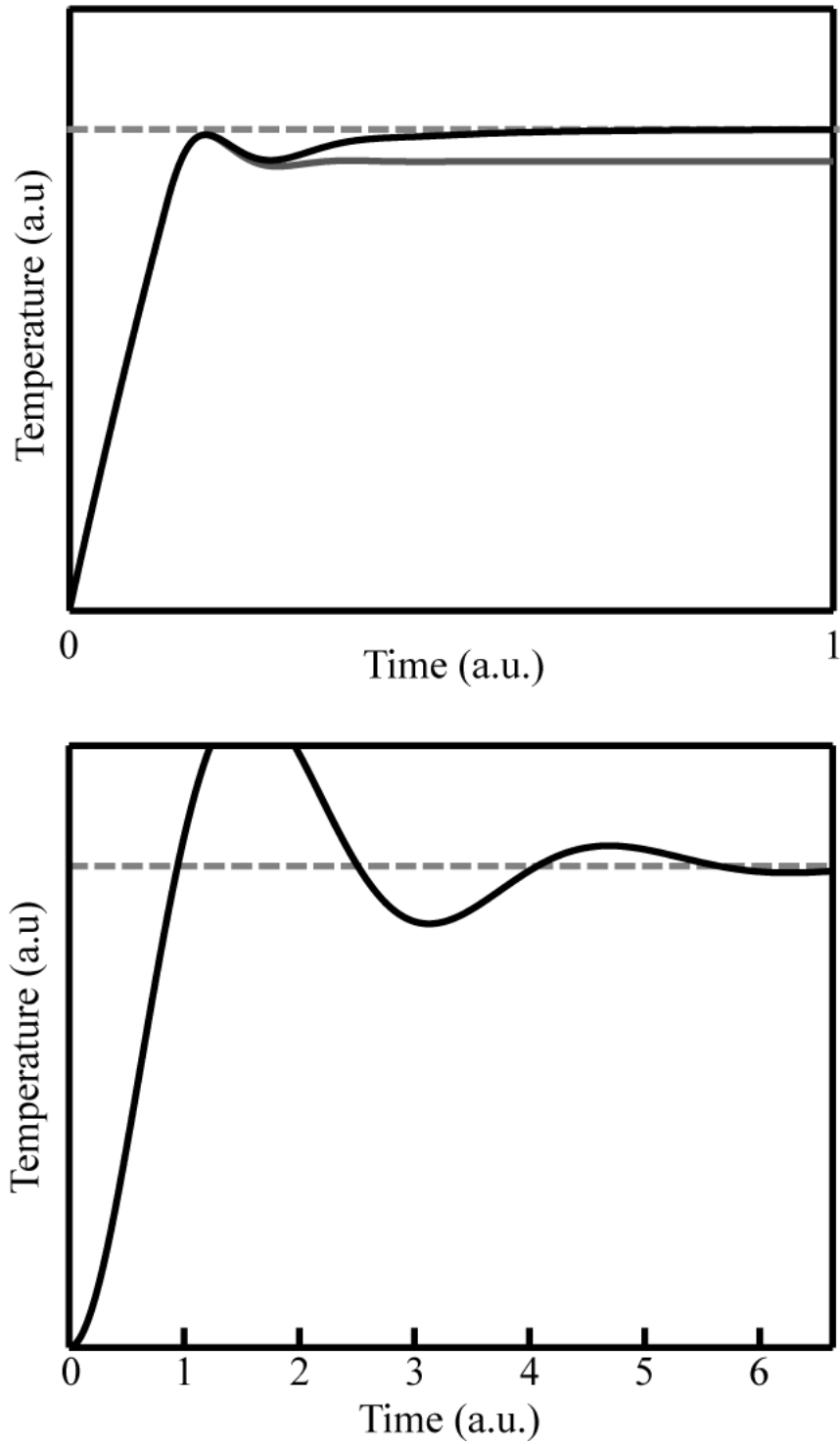


Figure 5.3: *Top:* A numerical simulation of a low- k_p proportional controller (grey) is plotted in comparison to a simulation of a PI controller, which uses the same k_p (black). *Bottom:* A simulated integral controller which uses the same k_i as the black curve is plotted. Note the difference in time axis between plots, and note the eventual convergence of the PI and I controllers to the target temperature.

Target temperatures are often far from initial temperatures. During the initial, proportional control-dominated warming to the target temperature, a large value for the integral response can accumulate, which results in a large, initial spike above the target temperature. Because the proportional component can drive initial heating, integral control is not required at early times. The selective removal of the integral component at temperatures far removed from the target does not affect the stability of the control algorithm and eliminates the initial integral spike. The only additional parameter for refined integral control is a threshold, which specifies a quantitative criterion for the “nearness” of the temperature to the target. In our apparatus, the most reliably stable indicator of nearness is the magnitude of the output signal excluding the integral component. Specifically, when the output voltage of the sum of proportional and derivative components is less than 8 V, the substrate temperature is evaluated as near enough to activate the integral component.

Figure 5.3 shows the results of numerical simulations using proportional, integral and proportional + integral control. The PI controller is shown with a threshold for the initiation of integral control. The controls with an integral component arrive at the specified target temperature, in contrast to a purely proportional control algorithm. However, the integral component equilibrates rather sluggishly, and a PI controller approaches the target temperature relatively slowly. A more advanced control algorithm is required to quickly approach a desired target temperature.

5.3.3 Derivative Response

Derivative control produces an output (D) proportional to the slope of the difference between the sample temperature (T) and the preset, target temperature (T_0) with respect to time. The proportionality is determined by a constant (k_D). Equation 5.5 specifies the behavior of a derivative control device.

$$D = k_D \times \frac{d(T-T_0)}{dt} \quad (5.5)$$

The derivative output is added to the proportional and integral outputs. Unlike the proportional and integral control equations, no negative sign is required to define the derivative control equation with a positive k_D value. That is to say, the derivative component of the output works to oppose all temperature change, producing a positive output when the sample is cooling. The dissipative derivative component damps temperature oscillations and the initial overshoot of high- k_P and high- k_I controllers. Consequently, proportional or integral constants can be increased upon the addition of a derivative term. An increase of the proportional or integral response allows a quicker approach to the target temperature, while the derivative component mutes instabilities near the target temperature. Figure 5.4 shows the speed gain of PID control over PI control using numerical simulations. PID control allows sufficiently rapid attainment of a target temperature for the TPD experiments without significant initial overshoot.

At temperatures far removed from the target temperature, the effect of the derivative component is negligible. The insensitivity to the derivative component results from the maximum output of the heater. The heater response requested by proportional or PI control substantially exceeds the maximum heater output when the

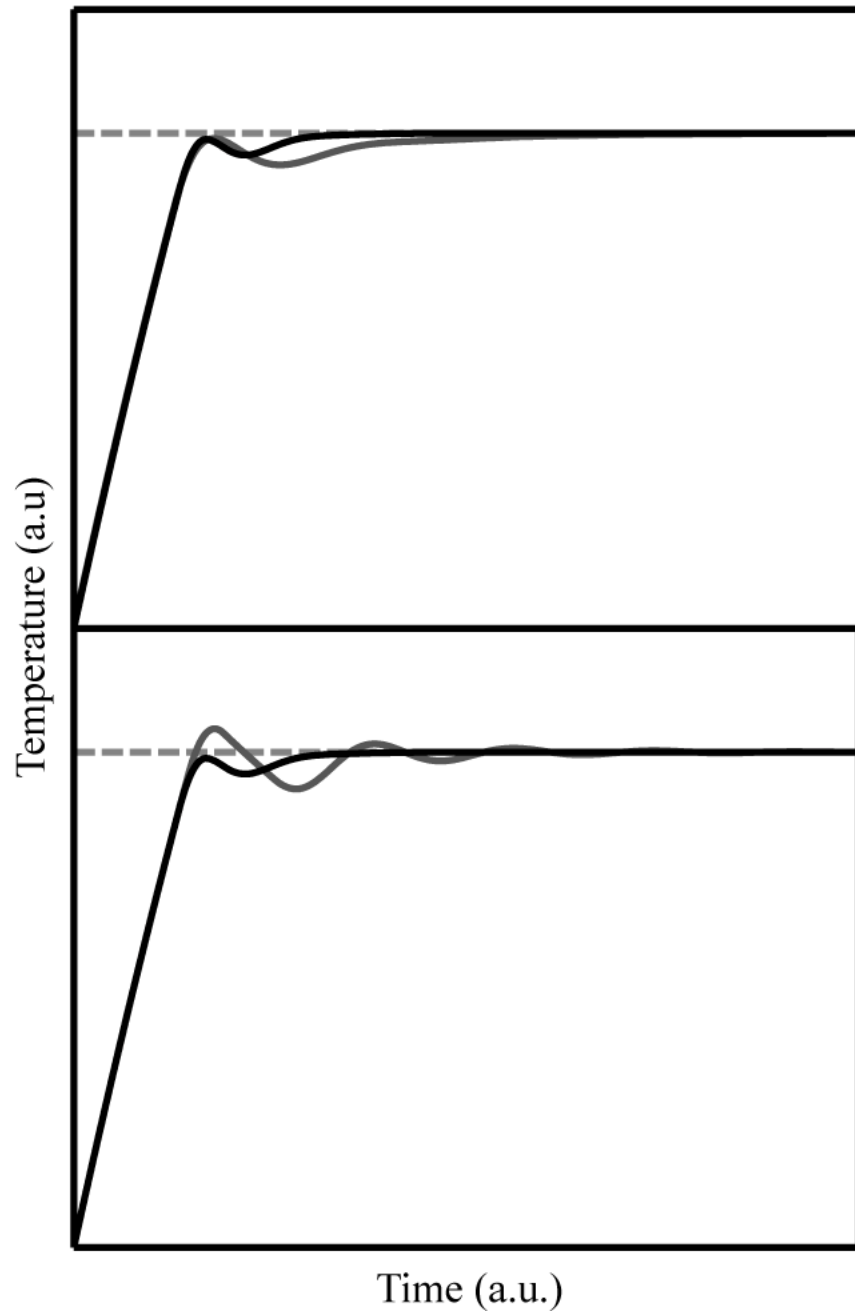


Figure 5.4: *Top*: A numerical simulation of an optimized PID controller (black) is compared to a simulation of an optimized PI controller (grey). The PID controller converges to the target temperature (dotted) much more quickly than the PI controller. *Bottom*: The optimized PID controller (black) from the upper panel is compared to a PI controller (grey) which uses the same k_p and k_i . The derivative damping allows use of larger k_p and k_i in the PID controller which would otherwise cause oscillations using PI control.

sample temperature is 15 K or more from the target temperature. As a result, the total PID output exceeds the maximum output unless the sample temperature is near the target temperature. Under the conditions of constant k_P and k_I , adjustment of k_D determines the magnitude of the D response and consequently sets the threshold temperature, at which the total PID response no longer exceeds the maximum heater output. Only at this temperature can the D component begin to slow the rate of heating. The value of k_D must be adjusted to lower the threshold temperature to a value that allows sufficient time for the influence of the D component to prevent an initial overshoot of temperature.

5.4 Software Implementation of PID Temperature Control

I have written multiple software implementations for PID temperature control in Labview. Two, stable software builds have been used during the course of my graduate work. The older build more intuitively implements the theory of PID control. It is explained for its pedagogical value. The newer build of the PID temperature control software can be best understood as an upgrade to the old build, which introduces resource-conserving conventions. Because both the mass spectrometer and the temperature control program are run from the same PC, and because the mass spectrometer software can collect data points at a quicker rate when more system resources are present, CPU and memory conservation were a design motivation for the newer software build.

5.4.1 Original Software Build

The original software build relied on a constant (100 – 1000 Hz) sampling of the thermocouple output. The temperature from each query of the thermocouple was stored in a chronological array. An additional array stored the time delay between thermocouple sampling events. The lengths of the arrays were determined by the component which required the largest sample of thermocouple data for computation: the integral component. When the arrays filled, the first elements of the arrays were discarded, and the value of every array element was transferred to the element before it. The new values were inserted in the newly vacant, last array elements, thus preserving the chronology of the array. This method was horribly computationally inefficient. An improved method of bookkeeping would have been to keep an index of the oldest array element. Upon each thermocouple sampling event, only the array value of that index would be replaced, and the index would be shifted by one. However, the software build outlined in Section 5.4.2 presents additional advantages; consequently, this improvement was not implemented.

To calculate proportional, integral and derivative responses, values from the arrays were used. Up to ten array elements were used for the averaging of components that were theoretically instantaneous, such as the proportional response, to remove some of the noise fluctuations in the thermocouple reading. The integral component required calculating the product of all temperature array elements with all time delay array elements *at every iteration*. Since the array length is finite, the integral response is necessarily somewhat truncated; however it fulfilled its function

by being temporally much longer than the proportional and derivative components.

The program allowed for on-the-fly adjusting of a number of parameters: the proportional, integral and derivative constants, the number of bins to be used in the integral component calculation, the number of bins to average for proportional and derivative components, and the high and low output limits. Additionally, the program contains a switch to turn temperature logging on and off. When temperature logging was activated, the average temperature from the previous 100 ms was saved to a text file with a time stamp. The low output limit was a necessary feature, and its value was not set to zero. It was determined that the power supply responded to temperature control outputs no less than 3.2 V. As a result, the low output limit, when set to 3.2 V, adds an offset of 3.2 V to the PID output. Temperature control after the installation of this feature was subsequently more stable.

5.4.2 Current Software Build

The conservation of CPU cycles was the primary motivation for a redesign of temperature control software, because the mass spectrometer can log data points more quickly with a larger share of CPU power. The previous software build used up to 80% of CPU cycles when the resources were idle to maintain a stable temperature. The current software build implements a number of computation-saving algorithms, which allow PID temperature control with less than 20% of CPU cycles.

The current build removes the computationally expensive shifting of all array values at every iteration. However, a convention is implemented to remove the arrays

entirely while still preserving the necessary history of temperature values for PID control. The removal of the arrays greatly reduces the math that must be performed at every iteration, such as summing of all temperature-time delay products for the integral response. The convention that is introduced stores all relevant temperature information in one value. This is accomplished with running weighted averaging of the temperature. The temperature value obtained from a sampling event (T_i) is incorporated into the running weighted average temperature (T'_{rwa}) to generate a new running weighted average (T_{rwa}) with the following formula:

$$T_{rwa} = (1 - r_d) \times T_i + r_d \times T'_{rwa} \quad (5.6)$$

The parameter r_d is a value between zero and one, and it represents a decay rate.

The function of r_d can be more clearly illustrated by the definition of T'_{rwa} as it appears in Equation 5.6. Because of the iterative nature of the control program, T'_{rwa} can be expressed as the sum of all previous sampling events, with each event scaled by r_d to the appropriate degree.

$$T'_{rwa} = (1 - r_d) \times \sum_i (r_d)^{i-1} \times T_i \quad (5.7)$$

Here, i is an index representing the number of iterations of Equation 5.6 to which a particular temperature reading T has been subjected. From Equation 5.7, it can be seen that the magnitude of a particular temperature value, and thus its influence on T_{rwa} , diminishes upon multiple iterations. The iterative decay of a term approaches exponential decay as $i \rightarrow \infty$. The rate of decay is governed by the value of r_d , with values approaching one producing longer decay times, and running weighted averages can be discussed in terms of long (high r_d) and short (low r_d) duration. Effectively, the

adjustment of r_d is analogous to the adjustment of the array length in the old software build.

Unlike the array length in the old software build, the decay rate r_d is not a useful or intuitive quantity for use in PID control. Specifically, the r_d does not relate linearly or simply to the decay time of a particular measurement. Adjustment of r_d is accomplished by the software user through the adjustment of a quantity labeled ‘half-life’, measured in units of iterations. The half-life is calculated from the traditional definition as the number of iterations required to reduce an input value to half of its original magnitude. A value of the half-life can be obtained in units of iterations by solving for i in Equation 5.8:

$$T_i = T \times (r_d)^{i-1} \quad (5.8)$$

under the condition of $T_i = 0.5 \times T$. The half-life provides a much more intuitive connection to the array length as expressed in the old software. As an example, doubling the half-life from 75 iterations to 150 iterations produces a tiny change in r_d from 0.9907 to 0.9954. While r_d is the quantity used by the control program via Equation 5.6, the half-life is a much more accessible quantity for the end user.

The running weighted average provides a method by which the history of temperature sampling events is condensed into one value, and the half-life effectively determines the time over which the value is averaged. Only one computation, Equation 5.6, is required per iteration for a running weighted average! In practice, multiple averages are required for PID control, which reflects the differing timescales needed for computation of proportional, integral and derivative components. In the current software build, one, short average is used to remove temperature fluctuations

from the proportional response. A very long average is used for the integral response, with the value of the average tracking the $(T-T_0) \times dt$ product. Three averages are used in the calculation of the derivative component: an average is used for the value of dt , an average with the same half-life as the dt average is used for $(T-T_0)$, and an average with a half-life half of the other two components is used for an additional $(T-T_0)$ measurement. From the three averages, a $d(T-T_0)/dt$ term can be calculated.

In short, the computational load per iteration is much reduced in the new software build compared to the summing and multiplication of array elements. Additionally, the running weighted average method is completely scalable. The extension of the time, over which a variable is averaged, imposes no additional CPU or memory requirements, unlike the old software build.

5.5 Tuning the PID Controller to the Apparatus

The adjustment of k_P , k_I and k_D to provide a rapid, stable acquisition of a target temperature is a simple matter. Each adjustment of a proportionality constant is followed by the acquisition of a target temperature > 50 K above the substrate temperature, and the behavior of the controller is observed. First, the proportional response is varied with k_I and k_D set to zero. The threshold value of k_P is determined for the onset of the oscillatory behavior shown in Figure 5.2, and k_P is set slightly below this value. Next, the integral component is increased to a value slightly below the onset of additional oscillatory behavior. A derivative component is added, and the combination of proportional and derivative components is increased until additional

adjustments produce either oscillatory behavior or an initial spike above the target temperature. Finally, the integral component can be increased somewhat as a result of derivative damping. The result of the tuning procedure is a program capable of sub-Kelvin temperature fluctuations at the target temperature: without an initial temperature spike above the target, in times less than 10 s after the initial approach of the temperature within 10 K of the target.

5.6 Linear Temperature Ramping for TPD

The collection of easily-interpretable TPD spectra requires a linear ramp in substrate temperature. Modifications to the PID temperature control algorithm were considered, but a detailed ramp control program proved unnecessary. The rate of change of the substrate temperature with respect to time (dT/dt) is proportional to the total flux of heat from the substrate, as expressed in Equation 5.9:

$$\frac{dT}{dt} = \frac{dQ_{heater}}{dt} + \frac{dQ_{loss}}{dt} \quad (5.9)$$

where dQ_{heater}/dt and dQ_{loss}/dt are the respectively positive and negative heating rates induced by the heater and by loss of heat to the surrounding bath. As specified in Equation 5.2, dQ_{loss}/dt is dependent on the difference in temperature between the sample and the bath, which produces a temperature dependent dT/dt and a non-linear temperature ramp.

However, in the limit of $dQ_{heater}/dt \gg -dQ_{loss}/dt$, the ramp rate becomes quite linear when using a constant heater power. Operation of the heater near its maximum

output (35 – 45 W) produces temperature ramp rates between 1 – 3 K while using cryogenic cooling. Under these heating conditions, the temperature ramp rate has been empirically determined as quite linear under 400 K, and non-trivial deviations from linearity only emerge above 500 K. Effectively, $dQ_{heater}/dt \gg -dQ_{loss}/dt$ at all temperatures relevant to the thin films which we study. As a result, no advanced ramping algorithms were required for the experimental apparatus.

5.7 Summary

I have implemented a TPD apparatus with mass spectrometric detection in the UHV chamber. I have written a PID temperature control program for use with TPD measurements. The system provides rapid acquisition of target temperatures and a linear ramp rate at temperatures below 500 K. The efficiency of the PID algorithm allows sufficient CPU cycles for simultaneous, high-resolution collection of 3 – 5 mass/charge ratios by the mass spectrometer. The current implementation of TPD has proved useful in the characterization of many thin films by myself and coworkers.

References

1. Somorjai, G. A. *Principles of Surface Chemistry*, Prentice-Hall: New Jersey, 1972.
2. Stähler, J.; Mehlhorn, M.; Bovensiepen, U.; Meyer, M.; Kusmierek, D. O.; Morgenstern, K.; Wolf, M. *Phys. Rev. Lett.* **2007**, 98, 206105.
3. Gütde, J.; Berthold, W.; Höfer, U. *Chem. Rev.* **2006**, 106, 4261.
4. Szymanski, P.; Garrett-Roe, S.; Harris, C. B. *Prog. Surf. Sci.* **2005**, 78, 1 and references therein.
5. Hotzel, A. *Prog. Surf. Sci.* **2007**, 82, 336.
6. Zhao, J.; Li, B.; Onda, K.; Feng, M.; Petek, H. *Chem. Rev.* **2006**, 106, 4402.
7. Giesen, K.; Hage, F.; Riess, H. J.; Steinmann, W.; Haight, R.; Beigang, R.; Dreyfus, R.; Avouris, Ph.; Himpsel, F. J. *Phys. Scr.* **1987**, 35, 578.
8. Giesen, K.; Hage, F.; Himpsel, F. J.; Riess, H. J.; Steinmann, W. *Phys. Rev. Lett.* **1985**, 55, 300.
9. Chen, A. B.; Segall, B. *Solid State Commun.* **1976**, 18, 149.
10. Kevan, S. D.; Gaylord, R. H. *Phys. Rev. B.* **1987**, 36, 5809.
11. Miller, T.; McMahon, W. E.; Chiang, T.-C. *Phys. Rev. Lett.* **1996**, 77, 1167.
12. Miller, T.; Hansen, E. D.; McMahon, W. E.; Chiang, T.-C. *Surf. Sci.* **1997**, 376, 32.
13. Liu, S. H.; Miller, A. D.; Gaffney, K. J.; Szymanski, P.; Garrett-Roe, S.; Bezel, I.; Harris, C. B. *J. Phys. Chem. B* **2002**, 106, 12908.
14. McNeill, J. D. Ultrafast Dynamics of Electrons at Interfaces. Ph.D. Dissertation, University of California, Berkeley, CA, May 1999.
15. Shipman, S. T.; Garrett-Roe, S.; Szymanski, P.; Yang, A.; Strader, M. L.; Harris, C. B. *J. Phys. Chem. B* **2006**, 110, 10002.
16. Shipman, S. T. Spectroscopy of Condensed Phase Systems: Infrared Holeburning and Ultrafast Two-Photon Photoemission. Ph.D. Dissertation, University of California, Berkeley, CA, December, 2005.

17. Merry, W. R. Image Potential States at Metal-Dielectric Interfaces. Ph.D. Dissertation, University of California, Berkeley, CA, April 1992.
18. Smadici, S.; Mocuta, D.; Osgood, R. M. *Phys. Rev. B* **2004**, *69*, 035415 and references therein.
19. Dutton, G.; Pu, J.; Trulhar, D. G.; Zhu, X.-Y. *J. Chem. Phys.* **2003**, *118*, 4337.
20. Bezel, I.; Gaffney, K. J.; Garrett-Roe, S.; Liu, S. H.; Miller, A. D.; Szymanski, P.; Harris, C. B. *J. Chem. Phys.* **2004**, *120*, 845.
21. Fauster, T.; Reuss, C.; Shumay, I. L.; Weinelt, M. *Chem. Phys.* **2000**, *251*, 111.
22. Gaffney, K. J. Dynamics of Electrons Photoinjected into Organic Semiconductors and Aromatic-Metal Interfaces. Ph.D. Dissertation, University of California, Berkeley, CA, December 2001.
23. Stähler, J.; Gahl, C.; Bovensiepen, U.; Wolf, M. *J. Phys. Chem. B* **2006**, *110*, 9637.
24. Lingle, Jr. R. L.; Ge, N.-H.; Jordan, R. E.; McNeill, J. D.; Harris, C. B. *Chem. Phys.* **1996**, *205*, 191.
25. Garrett-Roe, S.; Shipman, S. T.; Szymanski, P.; Strader, M. L.; Yang, A.; Harris, C. B. *J. Phys. Chem.* **2005**, *109*, 20370.
26. Johns, J. E. University of California, Berkeley, CA. Personal Communication, 2005.
27. Castner, Jr. E. W.; Maroncelli, M. *J. Mol. Liq.* **1998**, *77*, 1.
28. Maroncelli, M.; MacInnis, J.; Fleming, G. R. *Science* **1989**, *243*, 1674.
29. Schmickler, W. *Chem. Phys. Lett.* **1995**, *237*, 152.
30. Horng, M. L.; Gardecki, J. A.; Papazyan, A.; Maroncelli, M. *J. Phys. Chem.* **1995**, *99*, 17311.
31. Wandelt, K. In *Thin Metal Films and Gas Chemisorption*; Wissmann, P., Ed.; Elsevier: Amsterdam, New York, 1987; p 280.
32. Strader, M. L.; Garrett-Roe, S.; Szymanski, P.; Shipman, S. T.; Johns, J. E.; Yang, A.; Muller, E.; Harris, C. B. The Ultrafast Dynamics of Image Potential State Electrons at the Dimethylsulfoxide/Ag(111) Interface. *J. Phys. Chem. C* in press.

33. Miller, A. D.; Gaffney, K. J.; Liu, S. H.; Szymanski, P.; Garrett-Roe, S.; Wong, C. M.; Harris, C. B. *J. Phys. Chem. A* **2002**, *106*, 7636.
34. Gaffney, K. J.; Wong, C. M.; Liu, S. H.; Miller, A. D.; McNeill, J. D.; Harris, C. B. *Chem. Phys.* **2000**, *251*, 99.
35. Ge, N.-H.; Wong, C. M.; Harris, C. B. *Acc. Chem. Res* **2000**, *33*, 111.
36. Ng, T. N.; Silveira, W. R.; Marohn, J. A. *Phys. Rev. Lett.* **2007**, *98*, 066101.
37. Villegas, I.; Weaver, M. J. *J. Phys. Chem.* **1997**, *101*, 10166.
38. Shen, X. J.; Kwak, H.; Mocuta, D.; Radojevic, A. M.; Smadici, S.; Osgood, R. M. *Phys. Rev. B* **2001**, *63*, 165403.
39. Miller, A. D.; Bezel, I.; Gaffney, K. J.; Garrett-Roe, S.; Liu, S. H.; Szymanski, P.; Harris, C. B. *Science* **2002**, *297*, 1163.
40. Ge, N.-H.; Wong, C. M.; Lingle, Jr. R. L.; McNeill, J. D.; Gaffney, K. J.; Harris, C. B. *Science* **1998**, *279*, 202.
41. Muntwiler, M.; Zhu, X.-Y. *Phys. Rev. Lett.* **2007**, *98*, 246801.
42. Repp, J.; Meyer, G.; Olsson, F. E.; Persson, M. *Science* **2004**, *305*, 493.
43. Garrett-Roe, S. Ultrafast Electron Dynamics at Dielectric/Metal Interfaces: Intraband Relaxation of Image Potential State Electrons as Friction and Disorder Induced Electron Localization. Ph.D. Dissertation, University of California, Berkeley, CA, December 2005.
44. Feulner, P.; Menzel, D. *J. Vac. Sci. Technol.* **1980**, *17*, 662.
45. Szymanski, P. Ultrafast Electron Solvation and Localization at Nitrile/Ag(111) Interfaces. Ph.D. Dissertation, University of California, Berkeley, CA, December 2004.
46. Bard, A. J.; Faulkner, L. R. *Electrochemical Methods*; John Wiley & Sons, Inc.: New York, NY, 1980; pp 488-549.
47. Kojima, H.; Bard, A. J. *J. Am. Chem. Soc.* **1975**, *97*, 6317.
48. Fawcett, W. R.; Levine, S. J. *Electroanal. Chem.* **1973**, *43*, 175.
49. Grahame, D. C. *Chem. Rev.* **1947**, *41*, 441.

50. Helmholtz, H. *Ann. Phys. Chem.* **1853**, 165, 211.
51. Gouy, G. *J. Phys. Radium* **1910**, 9, 457.
52. Chapman, D. L. *Phil. Mag.* **1913**, 25, 475.
53. Stern, O. *Z. Elektrochem.* **1924**, 30, 508.
54. Tanaka, M.; Gohda, Y.; Furuya, S.; Watanabe, S. *Jpn. J. App. Phys.* **2003**, 42, L766.
55. Schröter, C.; Roelfs B.; Solomun, T. *Surf. Sci.* **1997**, 380, L441.
56. Si, S. K.; Gewirth, A. A. *J. Phys. Chem. B* **2000**, 104, 10775.
57. Borkowska, Z.; Stimming, U. In *Structure of Electrified Interfaces*; Lipkowski, J., Ross, P. N., Ed.; VCH: New York, NY, 1993; pp 277-307.
58. Sass, J. K.; Lackey, D.; Schott, J.; Straehler, B. *Surf. Sci.* **1991**, 247, 239.
59. Borkowska, Z.; Stimming, U. In *Structure of Electrified Interfaces*; Lipkowski, J., Ross, P. N., Ed.; VCH: New York, NY, 1993; pp 309-400.
60. Weaver, M. J. *Int. J. Mass Spectrom.* **1999**, 182, 403.
61. Verdaquer, A.; Sacha, G. M.; Bluhm, H.; Salmeron, M. *Chem. Rev.* **2006**, 106, 1478.
62. Shirley, D. A. *Phys. Rev. B: Condens. Matter* **1972**, 5, 4709.
63. Ikemiya, N.; Gewirth, A. A. *J. Phys. Chem. B* **2000**, 104, 873.
64. Miller, A. D.; Gaffney, K. J.; Liu, S. H.; Szymanski, P.; Garrett-Roe, S.; Wong, C. M.; Harris, C. B. *J. Phys. Chem. A* **2002**, 106, 7636.
65. Steinfeld, J. I.; Francisco, J. S.; Hase, W. L. *Chemical Kinetics and Dynamics*; Prentice-Hall, Inc.: Englewood Cliffs, NJ, 1989; pp 27.
66. Standard, J. M.; Gregory, B. W.; Clark, B. K.; *J. Mol. Struct.* **2007**, 803, 103.
67. Lindstrom, C.; Dutton, G.; Quinn, D. P.; Zhu, X.-Y. *Isr. J. Chem.* **2005**, 45, 195.
68. Zhu, X.-Y. *Annu. Rev. Phys. Chem.* **2002**, 53, 221.
69. Bovensiepen, U.; Gahl, C.; Wolf, M. *J. Phys. Chem. B* **2003**, 107, 8706.

70. Redhead, P. A. *Vacuum* **1963**, *12*, 203.
71. Sexton, B. A.; Avery, N. R.; Turney, T. W. *Surf. Sci.* **1983**, *124*, 162.
72. Jenniskens, H. G.; Dorlandt, P. W. F; Kadodwala, M. F.; Kleyn, A. W. *Surf. Sci.* **1996**, 357, 624.
73. Zhou, X.-L.; Castro, M. E.; White, J. M.; *Surf. Sci.* **1990**, 238, 215.
74. Yang, M. C.; Rockey, T. J.; Pursell, D.; Dai, H. L *J. Phys. Chem. B* **2001**, *105*, 11945.
75. Behm, R. J.; Brundle, C. R.; Wandelt, K. *J. Chem. Phys.* **1986**, 85, 1061.
76. Huang, W. X.; White, J. M. *J. Phys. Chem.* **2004**, *108*, 5060.
77. Moore, J. H.; Davis, C. C.; Coplan, M. A. *Building Scientific Apparatus* Perseus Books: Cambridge, MA, 2003; pp 591 – 600.
78. Kleiber, M. *Science* **1972**, *178*, 1283.